1
Multielectron High Harmonic Generation: simple man on complex plane

Olga Smirnova and Misha Ivanov

1.1
Introduction

Attosecond Science has emerged with the discovery of coherent electron-ion colli-sions induced by a strong laser field, usually referred to as "re-collisions" (Corkum (1993)). This discovery was initiated by the numerical experiments of K. Schafer, J. Krause and K. Kulander (see Krause et al (1992)). The work by Corkum (1993) drew on the concepts developed in the earlier work of Brunel (1987, 1990) and Corkum et al (1989). It has also been predated by the concept of 'Atomic Antenna' (Kuchiev (1987)). With the benefit of the hindsight, we now see the work by Kuchiev (1987) as the earliest quantum counterpart of the classical picture developed by Corkum (1993) and Kulander et al (1993) [1].

The classical picture of strong-field-induced ionization dynamics is summarized as follows. Once ionization removes an electron from an atom or a molecule, this elec-tron finds itself in the strong oscillating laser field. The Newton equations show that, within one or few cycles after ionization, the oscillating electron can be driven back by the laser field to re-encounter the parent ion. During this re-encounter, referred to as re-collision, the electron can do many things: scatter elastically (diffract), scat-ter inelastically (excitation or ionization of the parent ion), or radiatively recombine into one of the ion's empty states. It is this latter process that we will focus on here. The classical picture is usually referred to as the three-step model, or the simple man model [2].

If the recombination occurs to the exact same state that the electron has left from,

---

[1] While the quantum vision of Kuchiev (1987) has predated the classical picture, at that time it has lacked striking clarity and transparency of the quantitative predictions of the classical model (Corkum (1993)) which linked several key and seemingly disparate strong-field phenomena: high harmonic generation, production of very high energy electrons, and extreme efficiency of double ionization. The history of this discovery is rich and interesting in its own right, and would have warranted a separate chapter. Our purpose here is different – we simply urge our reader to read the papers by Brunel (1987, 1990), Corkum et al (1989), Kuchiev (1987), Schafer et al (1993), as well as a seemingly unrelated paper of **?**.

[2] As far as one of us (M.I.) can remember, the latter term has been used by K. Kulander, K. Schafer and H.-G. Muller, who have contributed a lot to the development of this classical model.

2

then the phase of the emitted radiation is the same from one atom to another, leading to the generation of coherent radiation in the medium. This process is known as high harmonic generation (HHG). It produces tens of eV-broad coherent spectra and has two crucial applications. First, high harmonic emission is used to generate attosecond pulses of light (see e.g. Krausz and Ivanov (2009)), which can then be used in time-resolved pump-probe experiments. Second, ultra-broad coherent harmonic spectrum carries attosecond information about the underlying nonlinear response, which can be extracted. The second direction is the subject of high harmonic spectroscopy (see e.g. Smirnova et al (2009); Lein (2005); Baker et al (2006)) – a new imaging technique with the combination of sub-Angstrom spatial and atto-second temporal resolution.

In the language of non-linear optics, high harmonic generation is a frequency up-conversion process that results from the macroscopic response of the medium. The non-linear polarization is induced in the medium by the (i) response of atoms and molecules, (ii) response of free electrons, (iii) response of the guiding medium, etc. Here we focus on the theory of single atom or single molecule response. Description of macroscopic propagation effects, which determine how coherent radiation from different atoms or molecules add together, can be found in Gaarde and Schafer (2008).

From the famous simple man model to the recent multichannel model, we will try to guide you through the several landmarks in our understanding of high harmonic generation. We hope to provide recipes and insight for modelling harmonic response in complex systems. The chapter includes the following sections:

- 1.2 The **simple man model** of high harmonic generation (HHG);
- 1.3 Formal approach for one-electron systems;
- 1.4 **The Lewenstein model**: stationary phase equations for HHG;
- 1.5 Factorization of the HHG dipole: the simple man on a complex plane;
- 1.6 Analysis of complex trajectories;
- 1.7 **The photoelectron model** of HHG: improved 'simple man' picture;
- 1.8 Tackling multi-electron systems: **The multichannel model** of HHG;
- 1.9 Appendix A: The saddle point method;
- 1.10 Appendix B: Treating the cut-off region: regularization of the divergent saddle point solutions;
- 1.11 Appendix C: Finding saddle points for the Lewenstein model.

Atomic units $\hbar = m = e = 1$ are used everywhere, unless specified otherwise.

1.2
The simple man model of high harmonic generation (HHG)

Experiments in eighties and early nineties of the last century yielded an astounding result: shaken with sufficiently intense infrared laser radiation, atomic medium was found to up-convert the frequency of the driving infrared laser light by up to two orders of magnitude (see e.g. Huillier and Balcou (1993); Macklin and C. L. Gordon (1993)). The observed harmonic spectrum formed a long plateau, with many harmonic orders, followed by a sharp cut-off. This observation has to be placed in

the context of what has been routinely seen in the traditional nonlinear optics: in the absence of resonances, the nonlinear response would decrease dramatically with increasing harmonic order, and the harmonic numbers would hardly ever reach double digits, let alone form a plateau extending beyond N=101.

To generate very high harmonics of the driving frequency, the atom has to absorb lots of photons. Generation of harmonics with numbers like N=21, ..., 31,..., etc means that at least that many photons had to be absorbed by the atom or a molecule.

The minimal amount of photons required for ionization is $N_0 = I_p/\omega$, where I_p is ionization potential and ω is the infrared laser frequency. For $I_p \sim 12 - 15$ eV and 800 nm driving IR laser field (the standard workhorse in many HHG experiments), $N_0 \sim 10$. One would have thought that once ten or so photons are absorbed, the electron should be free. And since it is well-known that a free electron should not absorb any more photons, the emission should stop around $N = 11$ or so for typical experimental conditions, in stark contrast with experimental observations.

Why and how many more photons are absorbed? What is the underlying mechanism? The liberated electron oscillates in the laser field, and its instantaneous energy can be very high. Can this instantaneous electron energy be converted into the harmonic photons? Where is the source of non-linearity, if the free electron oscillates with the frequency of the laser field?

The physical picture that clearly answered these question is the classical three-step model. It is simple, remarkably accurate, and is also intrinsically sub-cycle: within one optical period an electron is (i) removed from an atom or molecule, (ii) accelerated by the oscillating laser field, and (iii) driven back to re-collide with the parent ion. This picture connects the key strong-field phenomena: above-threshold ionization, non-sequential double ionization and high harmonic generation. It reveals the source of non-linearity in HHG: the recombination of the accelerated electron with the ion.

How can one check that this mechanism is indeed responsible for HHG? The key thing to check is whether or not this picture explains the cut-off of the harmonic spectra, that is, the highest harmonic order that can be efficiently produced. Numerically, the empirical cut-off law was found to be $\Omega_{\max} = I_p + 3U_p$ (Krause et al and Kulander (1992)), where I_p is the ionization potential and U_p is the cycle-average energy of electron oscillations in the laser field. To calculate the classical cut-off, we should calculate the maximal instantaneous energy of the returning electron classically, but to do that we need to know the initial conditions for the electron just after ionization. These conditions are specified within the three-step (simple man) model of HHG, which makes the following assumptions:

- SM1: The electron is born in the continuum at any time within the quarter of the laser cycle;
- SM2: The electron is born near the ionic core (i.e. near the origin of the reference frame) with zero velocity;
- SM3: The electron returns to the ionic core (origin) and its instantaneous energy of return is converted into the harmonic photon.

The pull of the ionic core on the liberated electron is neglected in the model, which
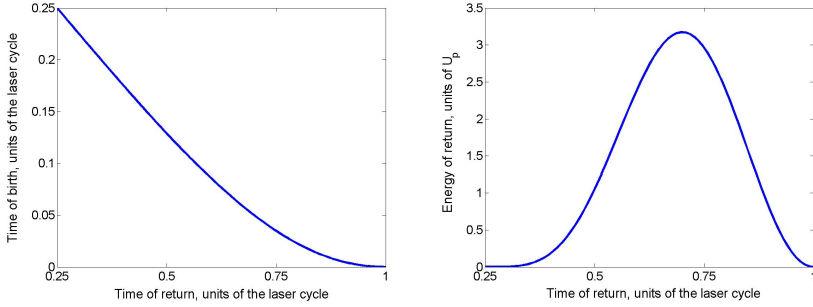
Figure 1.1 Window of classical 'birth' times and the return energy. Left panel: Time of birth vs. time of return. Right panel: Energy of electron at the time of return.

is not unreasonable given the very large excursions that the electron makes in the strong driving laser field. The possibility of the electron return to the core is dictated by the phase of the laser field at which it is launched on its classical orbit, and the time-window for the returning trajectories – the range of 'birth' times t_B – is shown in Fig. 1.1).

The calculation is done as follows: for each t_B we find the time of return t_R to the electron's original position (Fig. 1.1) and the energy at the moment of return (Fig. 1.1). Assumption that the strong laser field dominates the electron motion after ionization makes our calculations simpler. Once the ionic core potential is neglected, the kinetic momentum (velocity) at the time of birth t_B can be written as $\mathbf{k}(t_B) = \mathbf{p} + \mathbf{A}(t_B)$, where $\mathbf{p}$ is the electron canonical momentum and $\mathbf{A}(t)$ is the vector-potential of the laser field, which is related to the electric field $F(t)$ as $\mathbf{F}(t) = -\partial \mathbf{A}/\partial t$. The condition $\mathbf{k}(t_B) = 0$ (SM2) specifies $\mathbf{p} = -\mathbf{A}(t_B)$. Therefore, the electron kinetic momentum at all later times t is $\mathbf{k}(t) = -\mathbf{A}(t_B) + \mathbf{A}(t)$ and the electron energy at the time of return is

$$E_{\text{ret}}(t_R) = \mathbf{k}^2(t_R)/2 = (\mathbf{A}(t_B) - \mathbf{A}(t_R))^2/2 .$$

Zero displacement from t_B to t_R defines the return time t_R:

$$\int_{t_B}^{t_R} dt(\mathbf{A}(t) - \mathbf{A}(t_B)) = 0. \tag{1.1}$$

According to this model, the maximal return energy is about $3.17U_p$, where $U_p = F^2/4\omega^2$ is the cycle-average energy of the electron oscillations and F is the electric field amplitude. Then the maximum energy of the emitted harmonic photon is $3.17U_p + I_p$, where I_p is the binding energy of the ground state to which the electron recombines, in excellent agreement with the empirical cut-off law found numerically by Krause et al (1992).

The formal quantum approach considered in the next section will first take us away from the simple classical model. However, just like the recolliding electron revisits the ion, we will revisit the simple man model several times in this chapter, refining it at each step.

1.3
S-matrix expression for the HHG dipole (one electron)

The response of an individual atom or a molecule $P(\mathbf{r}, t) = nD(t)$ is proportional to the induced dipole $D(t)$:

$$\mathbf{D}(t) = \langle \Psi(t)|\hat{\mathbf{d}}|\Psi(t)\rangle, \tag{1.2}$$

where n is number density, $\hat{d}$ is the dipole operator, and $\Psi(t)$ is the wavefunction of the system obtained by solving the time-dependent Schroedinger equation (TDSE) with the Hamiltonian $\hat{H}(t)$:

$$i\partial\Psi(t)/\partial t = \hat{H}(t)\Psi(t). \tag{1.3}$$

We will first focus on single active electron approximation (see section 1.7 for the multielectron case). This approximation assumes that only one electron feels the laser field – the one that is liberated via strong-field ionization and recollides with the parent ion. All other electrons are frozen in the ion, unaffected by the laser field. The Hamiltonian of our system in the single active electron approximation is

$$\hat{H}(t) = \hat{\mathbf{p}}^2/2 + U(\mathbf{r}) + V_L(t), \tag{1.4}$$

where $\hat{\mathbf{p}} = -i\nabla\mathbf{r}$ is the momentum operator, $U(\mathbf{r})$ describes interaction of the electron with the ionic core, $V_L(t)$ describes the electron interaction with the laser field. In the dipole approximation and in the length gauge $\hat{V}_L(t) = -\hat{\mathbf{d}}\mathbf{F}(t) = \mathbf{F}(t)\mathbf{r}$ (see e.g. section 2.2.4 in the book by Grynberg *et al.* to learn about different gauges).

Formally, the solution of the Schroedinger equation (1.3) can be written in the integral form (see e.g. Smirnova et al and Ivanov (2007) for simple derivation):

$$|\Psi(\mathbf{r}, t)\rangle = -i \int_0^t dt' U(t, t')V_L(t')U_0(t', 0)|g\rangle + U_0(t, 0)|g\rangle, \tag{1.5}$$

where the ket-vector $|g\rangle$ represents the wave-function of the electron in the ground state $\Psi_g(\mathbf{r}) = \langle\mathbf{r}|g\rangle$, $U(t, t')$ is a full propagator, while $U_0(t', 0)$ is a field-free propagator. The propagators are the operators describing time-evolution of the wavefunction. The propagator $U_0(t', 0)$ is governing the electron dynamics from time 0 to time t' without the laser field, and is determined by the following equation:

$$i\partial U_0(t, 0)/\partial t = \hat{H}_0 U_0(t, 0), \tag{1.6}$$

$$U_0(0, 0) = 1, \tag{1.7}$$

$$\hat{H}_0 = \hat{\mathbf{p}}^2/2 + U(\mathbf{r}). \tag{1.8}$$

Symbolically, the solution of Eq.(1.6) can be written in compact form

$$U_0(t', 0) = e^{-i \int_0^{t'} \hat{H}_0(\xi) d\xi}. \tag{1.9}$$

where the integral is *time-ordered*, that is, the contribution of later times to the evolution follows the contribution of the earlier times.

The full propagator $U(t, t')$ governs the electron dynamics from time t' to the observation time t, driven by the combined action of the laser field and of the ionic core potential $U(\mathbf{r})$. It is given by

$$i\partial U(t, t')/\partial t = \hat{H} U(t, t'), \tag{1.10}$$

$$U(t, t') = e^{-i\int_{t'}^{t} \hat{H}(\xi) d\xi}, \tag{1.11}$$

$$U_0(t', t') = 1, \tag{1.12}$$

$$\tag{1.13}$$

The propagation without the laser field is straightforward. Denoting the of the ground state energy $E_g = -I_p$ (ionization potential) and the stationary ground state wave-function $\Psi_g(\mathbf{r})$, we have:

$$U_0(t', 0)\Psi_g(\mathbf{r}) = e^{iI_p t'} \Psi_g(\mathbf{r}). \tag{1.14}$$

The full propagator $U(t, t')$, on the other hand, is just as hard to find as the solution of the original equation (1.3). Thus, further approximations are required to make sense out of Eq.(1.5). The advantage of the integral expression is Eq.(1.5) is that making approximations is technically easier and physically more transparent.

Remembering that the laser field is strong, we can try to neglect the ionic potential in the full propagator. In this case the electron is free from time t' to time t. Its motion is only affected by the laser field and is described by the Hamiltonian $H_V(t) = \hat{\mathbf{p}}^2/2 + V_L(t)$. The corresponding approximation is called the Strong Field Approximation (SFA), and the propagator corresponding to $H_V(t)$ is often referred to as the Volkov propagator. The main advantage of the SFA is that the Volkov propagator can be found analytically. In the length gauge that we are using here, the result of acting with the Volkov propagator $U_V(t, t')$ on the plane wave with kinetic momentum $\mathbf{k}(t') = \mathbf{p} + \mathbf{A}(t')$ is

$$U_V(t, t')|\mathbf{p} + \mathbf{A}(t')\rangle = e^{-iS_V(\mathbf{p}, t, t')}|\mathbf{p} + \mathbf{A}(t)\rangle,$$

$$\langle \mathbf{r}|\mathbf{p} + \mathbf{A}(t)\rangle = e^{i(\mathbf{p} + \mathbf{A}(t))\mathbf{r}},$$

$$S_V(\mathbf{p}, t, t') = \frac{1}{2}\int_{t'}^{t} d\xi (\mathbf{p} + \mathbf{A}(\xi))^2, \tag{1.15}$$

That is, plane wave with the kinetic momentum $\mathbf{k}(t') = \mathbf{p} + \mathbf{A}(t')$ turns into the plane wave with the kinetic momentum $\mathbf{k}(t) = \mathbf{p} + \mathbf{A}(t)$ and accumulates the phase $S_V(\mathbf{p}, t, t')$ on the way.

Equations (1.15) define the Volkov function

$$\Psi_{\mathbf{p}}^{V}(\mathbf{r}, t) = e^{-iS_V(\mathbf{p}, t, t')} e^{i(\mathbf{p} + \mathbf{A}(t))\mathbf{r}} \quad .$$

Formally, the Volkov function is an eigen-state of the time-periodic Hamiltonian. It provides the quantum-mechanical description of the behavior of the free electron in the laser field. The coordinate part of the Volkov function is a plane wave, and these plane waves form complete basis at each moment of time:

$$\hat{1} = \int d\mathbf{p} |\mathbf{p} + \mathbf{A}(t)\rangle\langle \mathbf{p} + \mathbf{A}(t)|. \tag{1.16}$$

Within the SFA, the equation Eq.(1.5) takes the form

$$|\Psi(\mathbf{r}, t)\rangle = -i \int_0^t dt' U_V(t, t') V_L(t') U_0(t', 0)|g\rangle + U_0(t, 0)|g\rangle, \tag{1.17}$$

and can be solved analytically. The first term describes ionization, the second term describes evolution of the non-ionized part of the electron wave-function.

Thus, it is natural to associate t' with the time when ionization is initiated: before t' the electron is bound, after t' the electron is becoming free. Substituting equation (1.17) into Eq.(1.2) yields:

$$\mathbf{D}(t) \simeq -i\langle U_0(t, 0)g|\hat{\mathbf{d}}| \int_0^t dt' U_V(t, t')\hat{V}_L(t')U_0(t', 0)|g\rangle + cc. \tag{1.18}$$

Here we have assumed that there is no permanent dipole in the ground state and that the contribution of the continuum –continuum transitions to the dipole is negligible. The latter assumption is fine as long as ionization is weak. Thus, the dipole in the equation (1.18) is evaluated between the bound and the continuum components of the same wave-function.

The propagator $U_V(t, t')$ is known when it acts on the Volkov states. Thus, we introduce the identity operator resolved on the Volkov states Eq.(1.16) into Eq.(1.18):

$$\mathbf{D}(t) = -i\langle g|\hat{\mathbf{d}}| \int_0^t dt' e^{iI_p(t'-t)} \times$$

$$\times \int d\mathbf{p} U_V(t, t')|\mathbf{p} + \mathbf{A}(t')\rangle\langle\mathbf{p} + \mathbf{A}(t')|\hat{V}_L(t')|g\rangle + cc. \tag{1.19}$$

Finally, remembering that $\hat{V}_L(t) = -\hat{\mathbf{d}}\mathbf{F}(t)$, we re-write Eq.(1.19) in the compact form:

$$\mathbf{D}(t) = i \int_0^t dt' \int d\mathbf{p}\mathbf{d}^*(\mathbf{p} + \mathbf{A}(t))e^{-iS(\mathbf{p},t,t')}\mathbf{F}(t')\mathbf{d}(\mathbf{p} + \mathbf{A}(t')), \tag{1.20}$$

where we have introduced the dipole matrix elements $\mathbf{d}(\mathbf{p} + A(t))$ of the transitions between the ground state and the plane wave continuum,

$$\mathbf{d}(\mathbf{p} + \mathbf{A}(t)) \equiv \langle\mathbf{p} + \mathbf{A}(t)|\hat{\mathbf{d}}|\Psi_g(\mathbf{r})\rangle. \tag{1.21}$$

The phase

$$S(\mathbf{p}, t, t') \equiv \frac{1}{2} \int_{t'}^t (\mathbf{p} + \mathbf{A}(\tau))^2 d\tau + I_p(t - t') \tag{1.22}$$

is often referred to as action, and we will use this term below, even though strictly speaking it is only the energy part of the full classical action.

The harmonic spectrum $I(N\omega)$ obtains from the Fourier transform of $\mathbf{D}(t)$:

$$\mathbf{D}(N\omega) = \int dt e^{iN\omega t}\mathbf{D}(t),$$

$$I(N\omega) \propto (N\omega)^4|D(N\omega)|^2. \tag{1.23}$$

Note that $S(\mathbf{p}, t, t')$ is large and the integrand is a highly oscillating function, which is an advantage for the analytical evaluation of this integral. The analytical approach (Lewenstein et al (1994)) is based on the saddle point method (see Appendix A), which is the mathematical tool for evaluating integrals from fast-oscillating functions. It provides the physical picture of high harmonic generation as a three step process involving ionization, propagation and recombination (Ivanov and Burnett (1996)). It also supplies the time-energy mapping (**?**Baker et al (2006)) crucial for attosecond imaging and it is the basis for the extension of the above approach beyond the SFA and beyond the single active electron approximation (see e.g. Smirnova et al (2009)).

Let us now focus on the analytical saddle point approach to HHG.

1.4
Stationary phase equations for HHG: The Lewenstein model

The goal of this section is to evaluate integral Eqs.(1.20,1.23) using the saddle point method (see Appendix A). We need to find saddle points for all three integration variables t', t and $\mathbf{p}$, i.e. points where the rapidly changing phase of the integrand has zero derivatives with respect to all integration variables.

There are two ways to deal with the integral Eqs. (1.20,1.23). First, one can treat it as the multi-dimensional integral, find the saddle points for all the integration variables 'in parallel', and then follow the multi-dimensional saddle point approach to deal with the whole multi-dimensional integral 'at once'.

One can also take a different route and evaluate the multidimensional integral (1.20,1.23) step by step, sequentially. First, we find the saddle points t_i for the integral over t' from the saddle point equation:

$$\frac{dS}{dt'} \equiv \frac{\partial S(t', \mathbf{p}, t)}{\partial t'} = 0 \tag{1.24}$$

where the phase S is given by Eq.(1.22). We then evaluate the integral over t' treating it as a one-dimensional integral, with $\mathbf{p}$ and t entering as fixed parameters.

Next, we move to the integral over $\mathbf{p}$. Dealing with its saddle points, we should keep in mind that the saddle points of the previous integral $t' = t_i \equiv t_i(\mathbf{p}, t)$ depend on $\mathbf{p}$: $\frac{\partial t_i}{\partial p_\alpha} \neq 0, \alpha = x, y, z$.

Fortunately, thanks to Eq.(1.24), the explicit dependence of $t_i(\mathbf{p}, t)$ on $\mathbf{p}$ does not affect the position of the saddle points for the $\mathbf{p}$-integral:

$$\frac{dS(t_i, \mathbf{p}, t)}{dp_\alpha} \equiv \frac{\partial S(t_i, \mathbf{p}, t)}{\partial p_\alpha} + \frac{\partial S(t_i, \mathbf{p}, t)}{\partial t_i} \frac{\partial t_i}{\partial p_\alpha} = \frac{\partial S(t_i, \mathbf{p}, t)}{\partial p_\alpha} = 0 \tag{1.25}$$

Note, that the integral over $\mathbf{p}$ is treated as multidimensional, which leads to a slightly different pre-factor (see Appendix A).

Finally, we deal with the integral over t. Here, again, the saddle points $\mathbf{p}_s(t_i, t)$ depend on t: $\frac{\partial p_{s,\alpha}}{\partial t} \neq 0$. But once again the explicit dependence of $\mathbf{p}_s(t_i, t)$ on t does not affect the position of the saddle points thanks to Eq.(1.25):

$$\frac{dS(t_i, \mathbf{p}_s, t)}{dt} \equiv \frac{\partial S(t_i, \mathbf{p}_s, t)}{\partial t} + \frac{\partial S(t_i, \mathbf{p}_s, t)}{\partial p_\alpha} \frac{\partial p_\alpha}{\partial t} = \frac{\partial S(t_i, \mathbf{p}, t)}{\partial t} = 0 \tag{1.26}$$

The fact that both routes yield the same saddle point equations is not, of course, surprising – one should not be getting different answers depending on how the integral is evaluated.

Using Eq.(1.22), one obtains explicit form of equations (1.24,1.25, 1.26) which define the saddle points t_i, $\mathbf{p}_s$, t_r:

$$\frac{[\mathbf{p}_s + \mathbf{A}(t_i)]^2}{2} + I_p = 0, \tag{1.27}$$

$$\int_{t_i}^{t_r} [\mathbf{p}_s + \mathbf{A}(t')]dt' = 0, \tag{1.28}$$

$$\frac{[\mathbf{p}_s + \mathbf{A}(t_r)]^2}{2} + I_p = N\omega. \tag{1.29}$$

Here $\mathbf{p}_s$ is the electron drift (canonical) momentum, $\mathbf{k}_s(t) = \mathbf{p}_s + \mathbf{A}(t)$ is the kinetic momentum (the instantaneous electron velocity, up to the electron mass). The trajectories that satisfy Eqs. (1.28,1.27,1.29) are known as quantum orbits ?Kop,?.

Equation (1.28) requires that the electron returns to the parent ion – the prerequisite for recombination. Indeed, the time-integral from electron velocity yields electron displacement from t_i to t_r. Equation (1.28) dictates that the displacement is equal to zero.

Whereas Eq.(1.29) describes energy conservation during recombination, Eq.(1.27) describes tunnelling. It shows that the electron's kinetic energy at t_i is negative, its velocity $\mathbf{k}_s(t_i) = \mathbf{p}_s + \mathbf{A}(t_i)$ is complex, and hence $t_i = t_i' + t_i''$ is also complex – the hallmarks of the tunnelling process.

The time t_i can be identified with the moment when electron *enters the barrier*. Its *real part* will then correspond to the time when the electron *exits the barrier*. The origin of this concept will be explained in the next section.

The electron displacement during this "under barrier" motion from t_i to $\mathrm{Re}t_i$ is, in general, complex. Whether we like it or not, in general it yields complex coordinate of 'exit' $\mathbf{r}_{ex} = \mathbf{r}_{ex}' + i\mathbf{r}_{ex}''$ at $\mathrm{Re}t_i \equiv t_i'$:

$$\int_{t_i}^{t_i'} [\mathbf{p} + \mathbf{A}(t')]dt' = \mathbf{r}_{ex}' + i\mathbf{r}_{ex}''. \tag{1.30}$$

As a result, equations (1.28) and (1.29) can not be satisfied unless $\mathbf{p}$ or t_r are complex. Indeed, t_r must be complex to compensate the imaginary displacement accumulated under the barrier. However, the energy conservation law Eq. (1.29) dictates that $\mathbf{k}_s(t_r) = \mathbf{p}_s + \mathbf{A}(t_r)$ is real at the moment of recombination. Therefore, $\mathbf{p}_s$ must also be complex to compensate the imaginary part of $\mathbf{A}(t_r)$.

Thus, we are forced to conclude that, in contrast to the classical trajectories of the simple man model, the quantum orbits are the trajectories with complex canonical momenta, complex velocities, and complex displacements. These trajectories evolve in complex time. The only quantity that is required to be real is the one we measure – the energy of the emitted photon Eq. (1.29). Later in this Chapter, we will see when and how one can replace these trajectories with a different set, which does not involve complex canonical momenta and better corresponds to the classical picture. But for the moment, let us deal with the problem at hand.

For linearly polarized field, it is convenient to rewrite Eqs. (1.28,1.27,1.29) in terms of electron momenta parallel $p_{s,\parallel}$ and perpendicular $p_{s,\perp}$ to the polarization vector of the laser field:

$$\frac{[p_{s,\parallel} + A(t_i)]^2}{2} + I_{p,\text{eff}} = 0, \tag{1.31}$$

$$\int_{t_i}^{t_r} [p_{s,\parallel} + A(t')]dt' = 0, \qquad \int_{t_i}^{t_r} p_{s,\perp} dt' = 0, \tag{1.32}$$

$$\frac{[p_{s,\parallel} + A(t_r)]^2}{2} + I_{p,\text{eff}} = N\omega, \tag{1.33}$$

where we have introduced an "effective" ionization potential: $I_{p,eff} = I_p + p_{s,\perp}^2/2$. Eqs.(1.32) dictate that the stationary perpendicular canonical momentum is equal to zero for the linearly polarized field, $p_{s,\perp} = 0$. Then, Eqs.(1.32,1.31,1.33) reduce to a simpler set:

$$\frac{[p_{s,\parallel} + A(t_i)]^2}{2} + I_p = 0, \tag{1.34}$$

$$\int_{t_i}^{t_r} [p_{s,\parallel} + A(t')]dt' = 0, \tag{1.35}$$

$$\frac{[p_{s,\parallel} + A(t_r)]^2}{2} + I_p = N\omega, \tag{1.36}$$

Separating real and imaginary parts in Eqs.(1.34,1.35,1.36), we obtain six equations for six unknowns: $t_i = t_i' + it_i''$, $t_r = t_r' + it_r''$, $p_{s,\parallel} = p' + ip''$. Our goal is to solve these equations for each harmonic order N. Here is one way to do it, which we find simple and visually appealing.

First, we use Eqs.(1.34,1.36) to express all variables via the real t_r' and imaginary t_r'' return times. This can be done analytically. Second, we substitute the result into real and imaginary parts of equation Eq.(1.35):

$$F_1(N, t_r', t_r'') = \text{Re}\left[\int_{t_i}^{t_r} [p_{s,\parallel} + A(t')]dt'\right] = 0, \tag{1.37}$$

$$F_2(N, t_r', t_r'') = \text{Im}\left[\int_{t_i}^{t_r} [p_{s,\parallel} + A(t')]dt'\right] = 0. \tag{1.38}$$

Third, we solve equations (1.37,1.38) to find the only two remaining unknowns: real t_r' and imaginary t_r'' return times. While Eqs.(1.37,1.38) can not be solved analytically, dealing with two equations is much easier than with the original six.

Solving Eqs. (1.37,1.38) means that we need to find minima of the two-dimensional surface $F(N, t_r', t_r'')$ defined in the plane of real t_r' and imaginary t_r'' return times:

$$F(N, t_r', t_r'') \equiv [F_1(N, t_r', t_r'')]^2 + [F_2(N, t_r', t_r'')]^2 = 0. \tag{1.39}$$

These minima can be easily found numerically using the gradient method. The advantage of using $F(N, t_r', t_r'')$ is the ability to visualize the solutions: simply plotting the surface Eq.(1.39), one can examine the positions of the minima versus the harmonic number N.
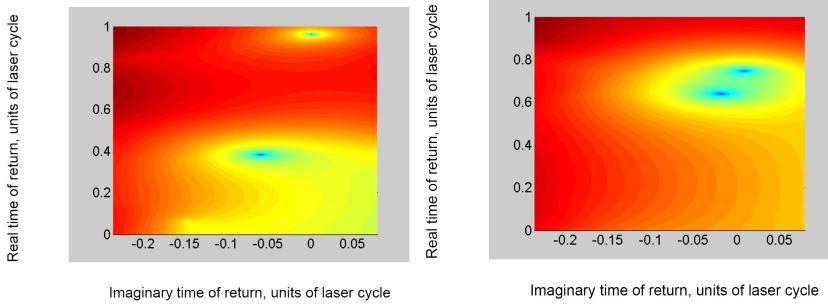
Figure 1.2 Surface (1.39) for $I_p =$15.6 eV, I=1.3 10^{14} W/cm^2. Left panel: $N = 11$ Two minima correspond to short ($\phi'_r \sim 0.4$) and long ($\phi'_r \sim 1$) trajectories. Right panel: $N = 27$ Two minima corresponding to short and long trajectories are merging together.

If we restrict our analysis to those solutions that lie within the same cycle of the laser field as the moment of ionization Ret_i, we will find two stationary solutions for each harmonic number N. These solutions are discussed in detail in the next section. They correspond to the two families of quantum orbits, called 'short' and 'long' trajectories. The trajectories merge for largest possible return energies, i.e. near the cut-off region of the harmonic spectrum.

There are also solutions that lie outside the laser cycle during which the electron was 'born' into the continuum. These 'super-long' trajectories describe second, third and higher-order returns of the electron to the origin. In typical experimental conditions, their contribution to the high harmonic emission is negligible thanks to the macroscopic effects – very long trajectories do not phase match well. Only very recently, the beautiful experiments of Zair et al (2008) have been able to clearly resolve the contributions of these trajectories, and their interference with the contribution from the long and short trajectories.

The stationary phase method for the integral over the return time t breaks down when these two stationary points merge and the second derivative of the action with respect to the return time is equal to zero $\partial^2 S/\partial t^2 = 0$. At this point, one needs to replace the standard saddle point method with the regularization procedure, discussed in the Appendix B.

Outside the cut-off region, up to a global phase factor the saddle point method yields the following expression for the harmonic dipole (1.20,1.23):

$$\mathbf{d}(N\omega) = \sum_{j=1}^{4M} \left[\frac{(2\pi)}{S''_{t_i,t_i}}\right]^{1/2} \left[\frac{(2\pi)}{S''_{t_r,t_r}}\right]^{1/2} \frac{(2\pi)^{3/2}}{\sqrt{\det(S''_{\mathbf{p}_s,\mathbf{p}_s})}} \times$$

$$\times \mathbf{d}^*(\mathbf{p}_s + \mathbf{A}(t_r))e^{-iS(\mathbf{p}_s,t_i,t_r)}\mathbf{F}(t_i)\mathbf{d}(\mathbf{p}_s + \mathbf{A}(t_i)), \tag{1.40}$$

where the Hessian $\det(S''_{\mathbf{p},\mathbf{p}})$ appears due to the multidimensional nature of the integral over $\mathbf{p}$. The sum runs over all stationary points for M periods of the laser light. Since there are two trajectories for each half-cycle of the laser field, i.e. for each ionization 'burst', and since there are 2M ionization bursts for M laser cycles, one has
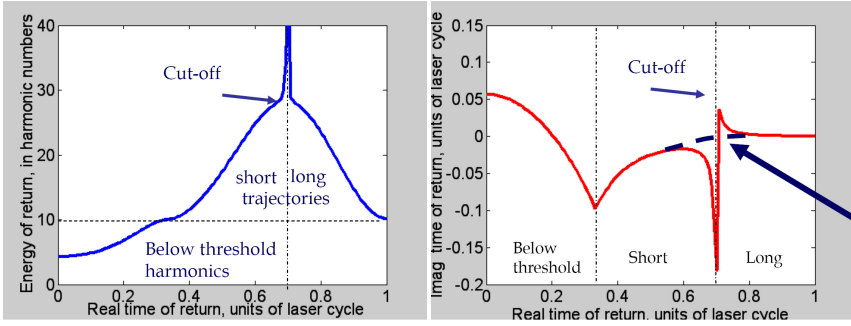
Figure 1.3 Left panel: Emission energy $E(t_r) + I_p = N\omega$ vs real time of return for $I_p = 15.6$ eV, I=1.3 10^{14} W/cm^2. Right panel: Imaginary time of return vs real time of return. The solution diverges in the cut-off region. Thick blue line schematically shows the desired outcome of regularization procedure.

$4M$ stationary points.

The above expression has one important caveat: the dipole matrix element $\mathbf{d}(\mathbf{p}_s + \mathbf{A}(t_i))$ is singular exactly at the saddle point $(\mathbf{p}_s + \mathbf{A}(t_i))^2/2 + I_p = 0$. The above expression pretends that there is no such singularity. Mathematically, the singularity reflects poles in scattering associated with the bound states of the system. A rigorous approach for dealing with this problem could be a subject of a separate chapter. A practical way of circumventing it is discussed later in this chapter.

1.5
Analysis of the complex trajectories

Let us now show how the above method of finding the saddle points works for linearly polarized laser field $F = F_0 \cos(\omega t)$, which corresponds to the vector potential $A = -A_0 \sin(\omega t)$. We shall introduce dimensionless variables $p_1 = \mathrm{Re} p_{s,\parallel}/A_0$, $p_2 = \mathrm{Im} p_{s,\parallel}/A_0$, $\phi_i = \omega t_i = \phi_i' + i\phi_i''$, $\phi_r = \omega t_r = \phi_r' + i\phi_r''$, $\gamma^2 = I_p/(2U_p)$, $\gamma_N^2 = (N\omega - I_p)/(2Up)$.

In terms of these variables, Eqs. (1.37,1.38) for the linearly polarized field yield:

$$F_1 = p_1(\phi_r' - \phi_i') - p_2(\phi_r'' - \phi_i'') - \cos(\phi_i')\cosh(\phi_i'') + \cosh(\phi_r'')\cos(\phi_r') = 0 \quad (1.41)$$
$$F_2 = p_1(\phi_r'' - \phi_i'') + p_2(\phi_r' - \phi_i') + \sin(\phi_i')\sinh(\phi_i'') - \sinh(\phi_r'')\sin(\phi_r') = 0 \quad (1.42)$$

Real and imaginary parts of Eq.(1.36) allow one to express real p_1 and imaginary p_2 components of the canonical momentum via real and imaginary parts of the return time (for above threshold harmonics):

$$p_1 = \cosh(\phi_r'')\sin(\phi_r') + \gamma_N, \quad (1.43)$$
$$p_2 = \sinh(\phi_r'')\cos(\phi_r'). \quad (1.44)$$

Real and imaginary parts of Eq.(1.34):

$$p_1 = \cosh(\phi_i'') \sin(\phi_i'), \tag{1.45}$$

$$p_2 + \gamma = \sinh(\phi_i'') \cos(\phi_i'). \tag{1.46}$$

allow one to express real ϕ_i' and imaginary ϕ_i'' ionization times via p_1 and p_2:

$$\phi_i' = \arcsin(\sqrt{(P-D)/2}), \tag{1.47}$$

$$\phi_i'' = \mathrm{arcosh}(\sqrt{(P+D)/2}), \tag{1.48}$$

where

$$P = p_1^2 + \tilde{\gamma}^2 + 1,$$

$$D = \sqrt{P^2 - 4p_1^2},$$

$$\tilde{\gamma} = \gamma + p_2 \tag{1.49}$$

Now we can use our recipe:

- Pick a grid of values ϕ_r', ϕ_r'' in the complex plane of return times ϕ_r;
- Pick a grid point ϕ_r', ϕ_r'' and calculate p_1, p_2 using Eqs.(1.43,1.44) and ϕ_i'' and ϕ_i' using Eqs.(1.47,1.48);
- Substitute ϕ_i'', ϕ_i', p_1, p_2 into equations (1.41,1.42);
- Plot the function $F \equiv F_1^2 + F_2^2$ in the plane of real and imaginary return times;
- Look for the minima, see Fig.(1.2).

Instead of reading out the solutions from the graph, one can find the minima using the gradient method. An alternative algorithm using the same ideas is described in Appendix C.

The imaginary and real return times (Fig.1.3, left panel) define the integration contour in the complex plane: only along this contour the energy of return and therefore the energy of the emitted photon is real. This energy is shown in Fig.(1.3, right panel) vs the real component of the return time for typical experimental conditions.

The cut-off (maximal energy) corresponds to about $3.17U_p + 1.32I_p$ Lewenstein et al (1994). There are two different trajectories returning at different times that lead to the same recollision energy. Those returning earlier correspond to shorter excursion and are called 'short trajectories', those returning later are called 'long trajectories' as they correspond to larger excursions and longer travel times.

Fortunately for attosecond imaging, the contributions of the long and short trajectories to the harmonic emission separate in the macroscopic response: the harmonic light diverges differently for those trajectories, and thus the signal coming from short and long trajectories can be collected separately. As a result, each harmonic N is associated with a particular time-delay between ionization and recombination $t_r' - t_i'$ and therefore each harmonic takes a snapshot of the recombining system at a particular moment of time. This time-energy mapping Lein (2005); Baker et al (2006) is the basis for attosecond time resolution in high harmonic spectroscopy.

As mentioned in the previous section, the stationary phase (saddle point) method for the integral over return times t breaks down near the cut-off, where the two stationary points (short and long trajectories) begin to coalesce and the second derivative
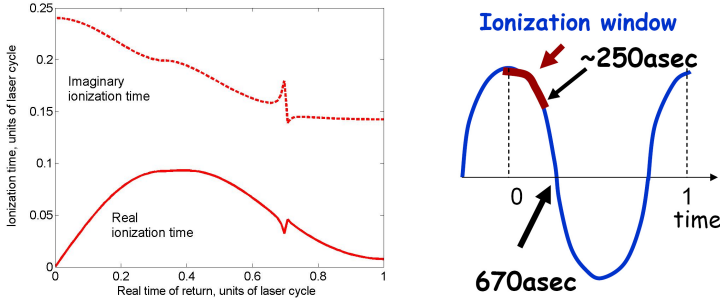
Figure 1.4 Left panel: Real and imaginary ionization times vs real return time for $I_p =$15.6 eV, I=1.3 10^{14} W/cm^2, $\omega = 1.5$ eV. Right panel: Cartoon illustrating the ionization window. Ionization occurs around field maximum within approximately 250 as window (corresponding to the maximum value of the real ionization time).

of the phase S with respect to return time is equal to zero, $\partial^2 S/\partial t^2 = 0$. The regularization of the solutions in the cut-off region is discussed in Appendix B. Here we shall proceed with the analysis of the stationary phase equations and turn to the ionization times.

The concept of ionization time together with the semiclassical (trajectories) perspective on ionization has been first introduced by V. Popov and co-workers (see Perelomov and Terent'ev (1966, 1967); Perelomov and Popov (1967); Popov and Perelomov (1968)). Just like in the Lewenstein model described above, the concept of trajectories arises from application of the saddle point method to the integral describing ionization:

$$a_{ion}(\mathbf{p},t) = -i \int_0^T e^{-iS(\mathbf{p},T,t')} \mathbf{F}(t')\mathbf{d}(\mathbf{p} + \mathbf{A}(t')). \tag{1.50}$$

Here the upper limit of the integral in the action (1.22) is the real time T, at which the liberated photoelectron is observed (detected).

The saddle point method applied to the SFA expressions yields the ionization amplitude:

$$a_{ion}(\mathbf{p},t) = \left[\frac{2\pi}{S''_{t_i,t_i}} \right]^{1/2} e^{-iS(\mathbf{p},T,t_i)} \mathbf{F}(t_i)\mathbf{d}(\mathbf{p} + \mathbf{A}(t_i)), \tag{1.51}$$

where t_i is the complex saddle point given by the condition

$$\frac{[\mathbf{p} + \mathbf{A}(t_i)]^2}{2} + I_p = 0, \tag{1.52}$$

Here we have dealt with the integral in the same way as when evaluating the harmonic dipole, pretending that corresponding dipole has no singularity at the saddle point. Note that the expression for the induced dipole Eq.(1.40) contains terms that look very much like the ionization amplitude. This observation is important, as it suggests the connection of the harmonic response to ionization, as in the simple-man model.

However, the story is more subtle: the stationary momenta p_s in the harmonic dipole are complex-valued, while here they are real observable quantities.

The integral (1.50) has been extensively studied by Keldysh, Popov, Perelomov, Terentev, and many others. The semiclassical picture in Perelomov and Terent'ev (1966, 1967); Perelomov and Popov (1967); Popov and Perelomov (1968) shows that strong-field ionization can be understood as tunnelling through the oscillating barrier, created by the laser field. The modulus of the ionization amplitude is associated with the imaginary part of the action S in Eq.(1.51). This imaginary part is only accumulated from t_i to t_i', since in the photoionization problem the canonical momentum registered at the detector is real and the integration over time also proceeds along the real time axis between t_i' and the observation time t.

This is why complex saddle point t_i is associated with time at which the electron enters the classically forbidden region – the tunnelling barrier, while the real part of the complex saddle point t_i', after which any changes to the ionization amplitude stop, is associated with the time of exit from the classically forbidden under-barrier region. The same reasoning can be extended to ionization times (Fig.1.4) arising within semiclassical picture of harmonic generation. However, ionization times in high harmonic generation are somewhat different due to complexity of $\mathbf{p}_s$. In the next section we will consider the connection between these two times.

Imaginary ionization time defines the ionization probability. Since the imaginary component of the ionization time is larger for short trajectories, these trajectories have lower chance of being launched compared to the long ones. The range over which the real part of the ionization time changes within the quarter-cycle defines the duration of the "ionization window". Typically, for $\lambda \simeq 800$ nm driving laser field and $I \sim 10^{14}$ W/cm^2 laser intensity, the ionization times (their real part) are spread within about 250 attoseconds around the instantaneous maximum of the laser field. Thus, strong-field ionization is an intrinsically attosecond process. Note that the quantum 'ionization window' is shorter than the classical one (see Fig. 1.1), as according to the classical simple-man picture ionization happens at any phase of the laser field.

Fig.1.5 shows saddle point solutions for the electron canonical momentum. In photoionization, the electron canonical momentum is always real, since it is the observable registered at the detector. In contrast, in harmonic generation the observable registered at the detector is the emitted photon, and hence it is photon energy that must be real. As a result, the electron canonical momenta in HHG are complex. Electrons on long trajectories have very small imaginary canonical momentum. Therefore, it is a very good approximation to associate long trajectories with photoelectrons. Note that the maximum of the real canonical momentum is about $p_{\max} \simeq A_0$. In the photoelectron perspective $p_{\max}$ corresponds to energy $2U_p$ at the detector - the cut-off energy for the so-called direct photo-electrons, i.e. those that have not substantially changed their momentum after ionization.

The imaginary part of the canonical momentum can be quite large for short trajectories. The complex valued solutions not only for the ionization times, but also for the recombination times and the electron canonical momenta challenge our understanding of the underlying physical picture of harmonic generation. If the first
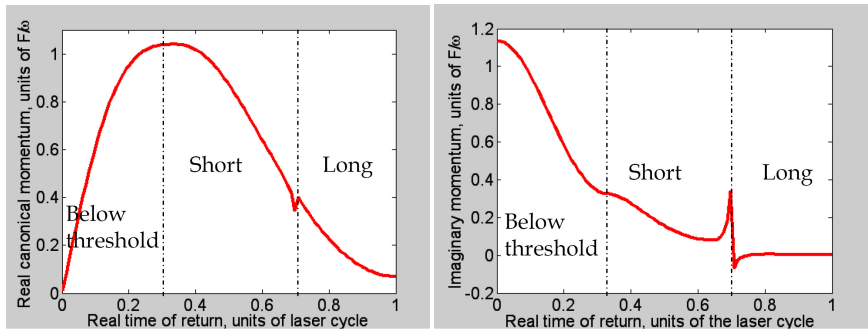
Figure 1.5 Left panel: real canonical momentum vs real return time for I_p =15.6 eV, I=1.3 10^{14} W/cm^2, $\omega = 1.5$ eV. Right panel: Imaginary canonical momentum vs real return time.

step of high harmonic generation is ionization, then why do these liberated electrons have complex canonical momenta? Does it mean that these electrons have not been ionized? Can we factorize the harmonic dipole into ionization, propagation and re-combination? The next section explores this opportunity.

1.6
Factorization of the HHG dipole: simple man on complex plane

Having derived analytical expressions for HHG dipole, can we identify the simple-man model in it, within the consistent quantum approach? To do this, we need to factorize the harmonic dipole into the three steps: ionization, propagation, recombination. That is, we have to re-write the dipole as a product of the ionization amplitude, the propagation amplitude and the recombination amplitude.

Such factorization of the harmonic dipole is not just curiosity driven. It is important for extending the modelling of harmonic emission to complex systems. Once the three steps are identified, the respective amplitudes can be imported from different approaches, tailored to calculate specifically ionization or recombination in complex systems. In particular, this will allow us to do away with the singularity still present in the dipole matrix element in Eq.(1.51).

Factorization of the harmonic dipole runs into two types of problems: technical and conceptual. The technical problems arise from the fact that the original three-step (simple man) model is formulated in time domain. The three processes – ioniza-tion, propagation and recombination – are the sequence of subsequent time-correlated events. The harmonic spectrum formally corresponds to the harmonic dipole in fre-quency domain, where the three processes become entangled: recall the contribution of different quantum trajectories to the same photon energy. Thus, rigorously fac-torization in frequency domain is only possible in the cut-off region where short and

long solutions merge Frolov et al (2009). [3].

The conceptual problem is due to the complex canonical momentum of the electron responsible for HHG. Photoelectrons associated with strong-field ionization have real momenta, since these momenta can be observed at the detector. Thus, ionization in terms of creating photoelectrons with real canonical momenta does not appear to fit into the HHG picture. Can we build an alternative model of HHG based entirely on the photoelectrons, i.e. electrons which are indeed ionized at the first step?

Let us address these issues step by step, starting with factorization of the harmonic dipole in frequency Frolov et al (2009); Kuchiev and Ostrovsky (1999); Morishita (2008) and time Ivanov and Burnett (1996) domains. The former involves factorization of equation (1.23), the latter factorizes equation (1.20).

1.6.1
Factorization of the HHG dipole in frequency domain

To re-write the harmonic dipole in the semi-factorized form, we can take Eq.(1.40) and split the action integral S that enters the phase of this expression into the three time intervals: from t_i to t_i', from t_i' to t_r', and from t_r' to t_r. Then we can identify the group of terms that looks like the ionization amplitude similar to that given by equation (1.51),

$$a_{ion}(\mathbf{p}_s, t_i) = \left[\frac{2\pi}{S_{t_i,t_i}''}\right]^{1/2} e^{-iS(\mathbf{p}_s, t_i', t_i)} \mathbf{F}(t_i)\mathbf{d}(\mathbf{p}_s + \mathbf{A}(t_i)), \qquad (1.53)$$

It is associated with the first time-interval, from t_i to t_i', and only the part of the action integral from t_i to the real time axis $t_i' = \mathrm{Re}t_i$ enters this amplitude. The momentum $\mathbf{p}_s$ is given by the full set of saddle point conditions for $t_i, t_r,$ and $\mathbf{p}_s$:

$$\frac{[p_s + \mathbf{A}(t_i)]^2}{2} + I_p = 0,$$

$$\int_{t_i}^{t_r} [\mathbf{p}_s + \mathbf{A}(t')]dt' = 0,$$

$$\frac{[\mathbf{p}_s + \mathbf{A}(t_r)]^2}{2} + I_p = N\omega, \qquad (1.54)$$

Now consider the next time interval, from t_i' to t_r'. The pre-factor arising from saddle point integration over the electron momenta $\mathbf{p}$ leads to the term

$$\frac{(2\pi)^{3/2}}{\sqrt{\det(S_{\mathbf{p}_s,\mathbf{p}_s}'')}} = \frac{(2\pi)^{3/2}}{(t_r - t_i)^{3/2}}.$$

This term describes free spreading of the electron wave-packet between t_i and t_r.

---

3) Note that the quantitative rescattering theory **??** postulates that one can factor out the recombination step in the frequency domain harmonic dipole. This postulate is supported by the results of numerical simulations demonstrating approximate factorization in the cut-off region Morishita (2008)
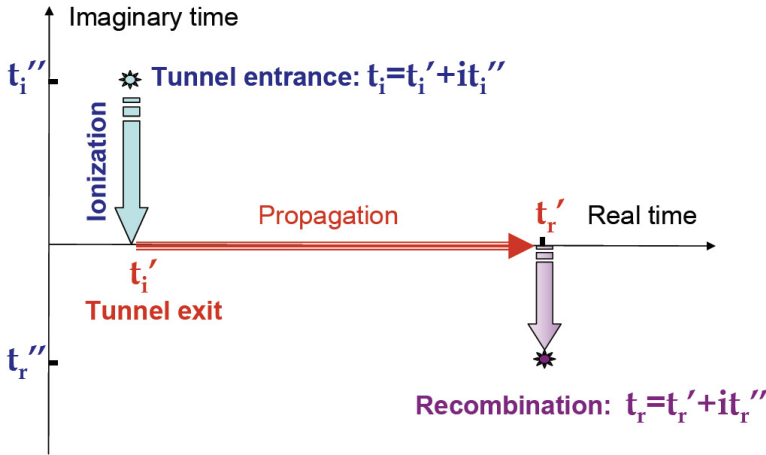
Figure 1.6 Contour of the time-integration in the action. Ionization occurs from complex time t_i to real time t_i'.

Thus, we associate the following group of terms with the propagation amplitude:

$$a_{prop} = \frac{(2\pi)^{3/2}}{(t_r - t_i)^{3/2}} e^{-iS(\mathbf{p}_s, t_r', t_i')}. \tag{1.55}$$

Note that the denominator includes complex-valued times t_i and t_r.

Finally, the recombination amplitude is represented by the recombination matrix element $d^*(\mathbf{p}_s + A(t_r))$ and can be associated with the following group of terms:

$$a_{rec} = \left[\frac{2\pi}{S_{t_r', t_r'}''} \right]^{1/2} e^{-iS(\mathbf{p}_s, t_r, t_r')} \mathbf{d}^*(\mathbf{p}_s + A(t_r)). \tag{1.56}$$

As a result, the total dipole is formally written as

$$d(N\omega) = \sum_{j=1}^{4M} a_{rec}(\mathbf{p}_s, t_r) a_{prop}(t_r, t_i) a_{ion}(\mathbf{p}_s, t_i), \tag{1.57}$$

However, in contrast with photoelectrons, electrons involved in HHG have complex canonical momentum $\mathbf{p}_s$. Therefore, the imaginary part of action is accumulated not only "under the barrier" from t_i to t_i', but also all the way between t_i' and t_r. Thus, factoring out ionization as the first step of HHG is not that convincing. Similarly, the recombination step involves not only the recombination dipole, but also possibly change in the amplitude due to the imaginary contribution to the action between t_r' and t_r. Thus, while we can formally associate several groups of terms in the harmonic dipole (1.57) with amplitudes of ionization, propagation and recombination, the complex-valued electron momenta make such identification somewhat artificial.

Additional point to note is that the three amplitudes are also entangled due to the sum over different saddle points in the equation (1.57). Even if we only consider contributions of the two most important trajectories, short and long, the sum entangles
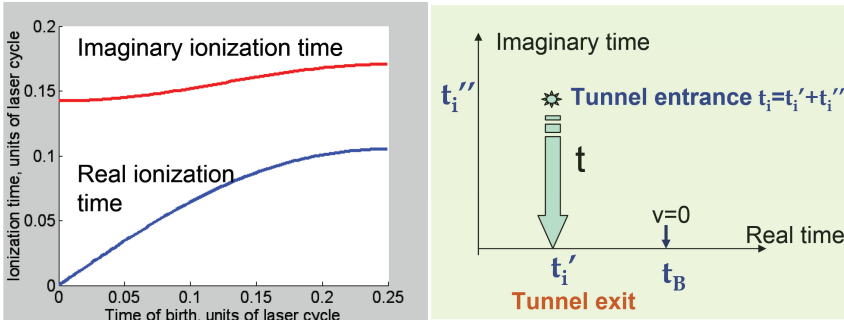
Figure 1.7 Left panel: Complex ionization time for photoelectrons t_i^{ph} vs time of birth for $I_p =$15.6 eV, I=1.3 10^{14} W/cm^2, $\omega = 1.5$ eV. Right panel: Cartoon illustrating the connection between t_i^{ph} and t_B: electron exits the barrier with the negative velocity (directed towards the core). Its velocity gradually decreases and becomes zero at classical ionization time - time of birth t_B.
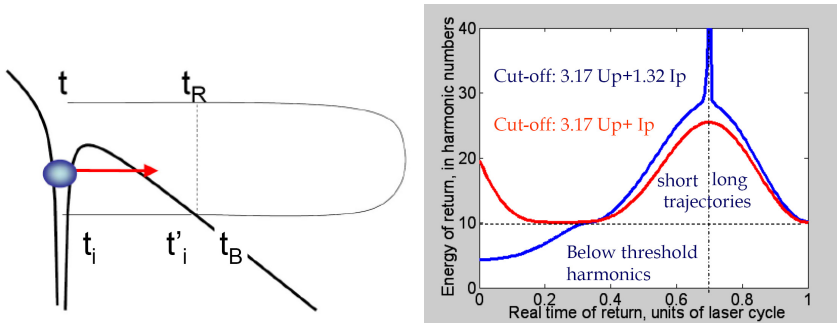
Figure 1.8 Left panel: real canonical momentum vs real return time for $I_p =$15.6 eV, I=1.3 10^{14} W/cm^2, $\omega = 1.5$ eV. Right panel: Imaginary canonical momentum vs real return time.

their contributions and also mixes up the contributions from different half-cycles. Importantly, finite pulse duration leads to different mapping between the given harmonic number and the ionization-recombination times for each half-cycle.

These technical problems can be remedied by looking at the dipole in time domain.

1.6.2
Factorization of the HHG dipole in time domain

There are several advantages to using time-domain dipole. For starters, if we do not perform the Fourier transform analytically, the time t_r no longer has to be complex. With the Fourier integral performed using standard FFT routine, we can keep t_r on the real time axis. The number of saddle-point conditions is also conveniently reduced

to two (one of them, for the momentum $\mathbf{p}_s$, is in general 3D)

$$\frac{[p_s + \mathbf{A}(t_i)]^2}{2} + I_p = 0,$$

$$\int_{t_i}^{t_r} [\mathbf{p}_s + \mathbf{A}(t')]dt' = 0, \tag{1.58}$$

with t_r being a parameter, instead of the harmonic number N.

In time domain, it is natural to sort contributions to the induced dipole according to the corresponding ionization bursts. Then, for each half-cycle j, there is a single ionization burst that contributes to the induced dipole as a function of the real return time t_r, see right panel of Fig. (1.4). After saddle-point integration, this contribution is:

$$\mathbf{D}_j^{hc}(t_r) = i \left[\frac{(2\pi)}{S''_{t_i,t_i}} \right]^{1/2} \frac{(2\pi)^{3/2}}{\sqrt{\det(S''_{\mathbf{p}_s,\mathbf{p}_s})}}$$

$$\times \mathbf{d}^*(\mathbf{p}_s + \mathbf{A}(t_r))e^{-iS(\mathbf{p},t_r,t_i)}\mathbf{F}(t_i)\mathbf{d}(\mathbf{p}_s + \mathbf{A}(t_i)),$$

$$S(\mathbf{p},t_r,t_i) \equiv \frac{1}{2}\int_{t_i}^{t_r}(\mathbf{p}_s + \mathcal{A}(\tau))^2 d\tau + I_p(t_r - t_i). \tag{1.59}$$

Just like in frequency domain, up to a global phase factor it can be written as a product of three amplitudes:

$$D_j^{hc}(t_r) = a_{rec}(\mathbf{p}_s,t_r)a_{prop}(t_r,t_i)a_{ion}(\mathbf{p}_s,t_i) \tag{1.60}$$

The ionization and propagation amplitudes entering this expression are given by Eqs. (1.53,1.55). As for the recombination amplitude, it is simply equal to the recombination matrix element $\mathbf{d}^*(\mathbf{p}_s + \mathbf{A}(t_r))$ (as we have not performed the Fourier transform yet). Equation (1.66) is the natural mathematical formulation of the three step model, which is intrinsically sub-cycle.

If we ignore multiple returns and very long trajectories, then for each t_r there is only one ionization burst to deal with. As opposed to frequency domain, the contributions of long and short trajectories from this ionization burst are not yet mixed – they are separated in time. This is very convenient if you need to look at the contribution of only short, or only long trajectories: it is straightforward to add a time-domain filter that would filter out the unwanted contributions. Essentially, this would correspond to making a window Fourier transform of the time-domain harmonic dipole. Including the contribution of multiple returns is rarely required for typical experimental conditions.

To model the full $d(t_r)$ one needs to model ionization, recombination and propagation separately for each half-cycle and then collect contributions from each half-cycle (each ionization burst):

$$d(t'_r) = \sum_j D_j^{hc}(t'_r). \tag{1.61}$$

To obtain the harmonic spectrum, we have to perform the Fourier transform, which is convenient to do numerically using the FFT routine. There are two possible approaches to implementing the Fourier transform.

Integration along the Lewenstein's contour. In this approach, the Fourier transform is performed along the time-contour in complex plane $t_r = t_r' + it_r''$. In this case the argument of the recombination dipole $\mathbf{p}_s + \mathbf{A}(t_r)$ remains real and so is the recollision energy $E_{rec}(t_r)$. Since it is difficult to *numerically* perform integration along a complex contour

$$d(N\omega) = \int dt_r e^{-(N\omega)t_r''} d(t_r) e^{iN\omega t_r'}, \tag{1.62}$$

one can use variable substitution and integrate over real return times t_r':

$$d(N\omega) = \int dt_r' \left[\frac{dt_r}{dt_r'} e^{-[E_{rec}(t_r)+I_p]t_r''} \right] d(t_r') e^{iN\omega t_r'}, \tag{1.63}$$

$$N\omega = E_{rec}(t_r) + I_p, \tag{1.64}$$

$$E_{rec}(t_r) = \frac{(\mathbf{p}_s + \mathbf{A}(t_r))^2}{2}. \tag{1.65}$$

The derivative in the square brackets is associated with the variable substitution.

Note that equation (1.63) contains one approximation: the term $e^{-(N\omega)t_r''}$ is modified according to the energy conservation $N\omega = E_{rec}(t_r) + I_p$. However, the integration of equation (1.63) is not very convenient due to additional effort associated with the need to avoid the divergence of $\frac{dt_r}{dt_r'}$ in the cut-off region (see Fig.1.3).

HHG dipole on the real time axis. To keep things simple one can keep the half-cycle harmonic dipole on the real time axis:

$$D_j^{hc}(t) = a_{rec}(\mathbf{p}_s, t) a_{prop}(t, t_i) a_{ion}(\mathbf{p}_s, t_i). \tag{1.66}$$

where the saddle points $\mathbf{p}_s$ and t_i are given by Eqs.(1.58).

In this 'real time-axis' approach the return time t is a parameter: we have to find t_i and $\mathbf{p}_s$ for each t. This can be done using the procedure similar to that described in the previous section, only simpler. Specifically, we introduce dimensionless variables $\phi = \omega t$ and $\mathbf{p}/(F/\omega) = p_1 + i\mathbf{p}_2$. For linearly polarized field $p_{s,\perp} = 0$. For each real ϕ we use equations (1.41,1.42) with $\phi_r'' = 0$ and $\phi_r' \equiv \phi$:

$$F_1(\phi) = p_1(\phi - \phi_i') + p_2\phi_i'' - \cos(\phi_i')\cosh(\phi_i'') + \cos(\phi) = 0, \tag{1.67}$$

$$F_2(\phi) = -p_1\phi_i'' + p_2(\phi - \phi_i') + \sin(\phi_i')\sinh(\phi_i'') = 0. \tag{1.68}$$

We can now express these functions in terms of real p_1 and imaginary p_2 components of $p_{s,\parallel}$ by substituting equations (1.47,1.48) for ϕ_i' and ϕ_i''. Alternatively, we can use Eqs.(1.45,1.46) to express p_1 and p_2 in terms of ϕ_i' and ϕ_i''. Either way, we build the surface $F(\phi) = F_1^2 + F_2^2$ and for each ϕ. Next, we find minima on this surface. If we use p_1 and p_2 as our variables, then these minima will yield us the real and imaginary p_2 components of the canonical momentum, and then equations (1.47,1.48) yield the corresponding ionization times.

Conveniently, in this approach the divergence at the cut-off is avoided, since the divergence occurs in the complex plane of return times when calculating the Fourier transform analytically. The price to pay is that the recombination dipole has to be taken at complex arguments $\mathbf{p}_s + \mathbf{A}(t)$ and the recollision energy $E_{rec}(t)$ has imaginary part. In practice, one can use the real part of the recollision energy as the

argument of the recombination dipole. If one wants to avoid this approximation, one has to extend recombination dipoles to the complex plane of electron momenta.

Thus, one can formally factorize the harmonic dipole in time domain overcoming technical problems associated with factorization. However, the conceptual problem associated with complex electron momenta and the definition of ionization still remains. Next section shows how, and to what extent, this problem can be circumvented. It introduces the photoelectron model of HHG, where the electron canonical momentum is restricted to the real axis.

1.7
The photoelectron model of HHG: the improved simple man

In the standard simple man model, the electron motion between ionization and recombination is modelled using classical trajectories. Naturally, the electron velocity, the ionization and recombination times are all real-valued quantities. In the quantum description, the rigorous approach based on the saddle point method leads to trajectories with complex-valued momenta, ionization and recombination times. The presence of complex canonical momentum makes it difficult to identify the ionization step.

Complex-valued canonical momenta and recombination times arise from the requirement that the electron returns exactly to its original position. Since the tunnelling electron accumulates imaginary displacement during its motion in the classically forbidden region, the complex-valued momenta and return times are there to compensate for this displacement.

This section shows that if we relax the return condition and neglect imaginary displacement between t_i and $\mathrm{Re} t_i$, we can obtain the same recollision energy for real-valued canonical momenta and real-valued return times. We shall call this approach the photoelectron model since it allows one to incorporate standard strong-field ionization concepts in a natural manner. The ionization amplitude would then correspond to creating an electron with real-valued canonical momentum, and the imaginary part of the action integral would only be accumulated between t_i and $\mathrm{Re} t_i$.

In the classical model, one assumes that the electron trajectory is launched at the real 'time of birth' t_B with zero instantaneous velocity. The electron momentum at t_B can be written as $\mathbf{k}(t_B) = \mathbf{p} + \mathbf{A}(t_B) = 0$, where the canonical momentum $\mathbf{p}$ is a constant of motion (neglecting the core potential). The link between t_B and $\mathbf{p}$, $\mathbf{p} = -\mathbf{A}(t_B)$, links t_B via $[\mathbf{p} + \mathbf{A}(t_i)]^2 = -I_p$ to the complex-valued ionization time t_i. In particular, for linearly polarized laser field we have $[(A(t_{i,ph}) - A(t_B)]^2 = -2I_p$. Note, that this $t_{i,ph}$ is in general different from the ionization time t_i introduced in the previous section, since now the electron canonical momentum is forced to be real. The notation $t_{i,ph}$ stresses that this ionization time corresponds to photoelectrons, i.e. electrons with real canonical momenta. Fig.1.7 shows the mapping between the time of birth and the complex time $t_{i,ph}$.

The photoelectron exits the tunnelling barrier at a real time $\mathrm{Re} t_{i,ph}$, and since $\mathrm{Re} t_{i,ph}$ turns out to be smaller than t_B, the electron velocity at $\mathrm{Re} t_{i,ph}$ is directed towards the core. It gradually decreases until becoming equal to zero at t_B. The
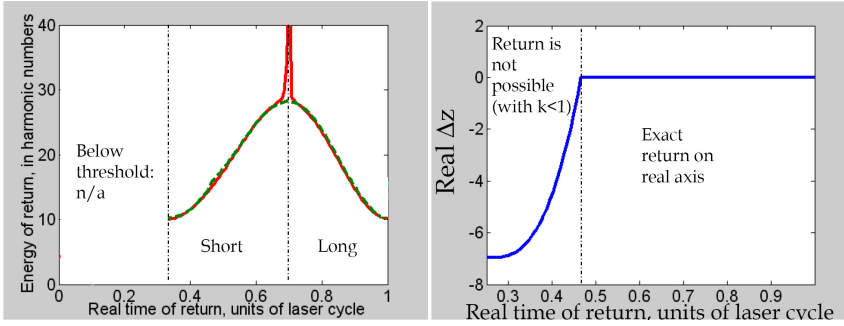
Figure 1.9 Left panel: Energy of return for the Lewenstein model (red) and photoelectron model (green) vs real return time for I_p =15.6 eV, I=1.3 10^{14} W/cm^2, $\omega = 1.5$ eV. Right panel: Real part of electron displacement in photoelectron model.

difference between $\mathrm{Re}t_{i,ph}$ and t_B is small near the peak of the oscillating electric field but increases as the field approaches zero. While the times t_B are always spread within one quarter-cycle, as in the classical model, the times $\mathrm{Re}t_{i,ph}$ are limited to a shorter fraction of the quarter-cycle, see Fig.1.7.

We now turn to classical return time t_R. In the original classical model it is defined by the condition

$$\int_{t_B}^{t_R} (p + A(\tau))d\tau = \int_{t_B}^{t_R} (-A(t_B) + A(\tau))d\tau = 0 \qquad (1.69)$$

However, since the electron is already offset from the origin at t_B

$$\Delta z = \int_{t_{i,ph}}^{t_B} d\tau(A(\tau) - A(t_B)) \qquad (1.70)$$

it does not return to the origin at t_R (see Fig.1.8). The energy $E(t_R) = ((A(t_R) - A(t_B))^2/2$ in the classical model is shown in Fig.1.8, with the cut-off at $3.17U_p + I_p$. The cutoff is lower than for the quantum treatment, precisely because the electron has not yet returned to the core. The extra $0.32I_p$ in the quantum cutoff law $3.17U_p + 1.32I_p$ is due to the extra energy accumulated by the electron while covering the extra displacement Δz [4].

Can we improve these results if we allow the photoelectrons to travel a bit longer and let them return to the core? Why don't we continue to monitor the electron trajectory at times $t > t_R$ and register their energy at the time of return to the origin $t_{r,ph}$, ignoring whatever imaginary displacement they might have. There is just one problem with this plan: not all trajectories will be able to return to the core since we have limited the canonical momentum $p_{ph} = -A(t_B)$ to be no more than A_0.

---

[4] Interestingly, if one defines the experimental cut-off using the classical model, then the classical time-energy mapping is very similar to the quantum: t_R is very close to the real part of t_r. Since in the experiment the intensity is rarely known exactly, it is very difficult to differentiate between the classical (red) and quantum (blue) return energies in Fig.1.8.

24

With this in mind, we shall take the energy at the closest approach to the origin as the return energy. We shall call this an improved three-step model or **the photoelectron model**.

The model implies neglecting the imaginary displacement and minimizing the real displacement between $t_{i,ph}$ and $t^{r,ph}$. The imaginary displacement has to be neglected since we do not have imaginary canonical momenta and imaginary return times to cover for it.

The photon energy resulting from the photoelectron model is $E_{rec}^{ph}(t) + I_p = \frac{dS}{dt_{r,ph}}$, where $S(p_{ph}, t_{i,ph}, t_{r,ph})$ is given by equation (1.22). It is in excellent agreement with the quantum photon energy (see Fig.1.9, left panel) for all trajectories where the real part of electron displacement from the origin passes through zero. This is the case for the long trajectories and for most of the short trajectories, except for the shortest ones. These latter are 'born' at the end of the ionization window and contribute to the lowest harmonics just above the ionization threshold.

For short trajectories, the electron is decelerated by the laser field while returning to the core. Therefore, it needs sufficiently high drift momentum to reach the origin. Since we have limited the canonical momentum $p = -A(t_B)$ below A_0, the shortest trajectories can not quite make it to the core. For them, the time $t_{r,ph}$ corresponds to the closest approach to the core. Non-zero real displacement yields deviation of the approximate action $S(p_{ph}, t_{i,ph}, t_{r,ph})$ from the real part of the exact action defined in the previous section, see Fig. (1.9, right panel).

Action in this model is reproduced very well since it is the time-integral from the photon energy. Once the electron return energy is well-reproduced, so is the action, even if the end points t_i', t_r' are shifted.

From the mathematical perspective, the photoelectron model implies that when we perform the integrals, we expand the action not at the exact saddle point, but in its vicinity. In particular, we shift the center of the expansion for the canonical momentum from the complex plane to the real axis. The error introduced in the integral by this procedure is minimized if the new expansion point lies within the saddle point region of the exact complex saddle point of the multi-dimensional integral. Thus, the difference $\Delta p = p_q - p_{ph}$ between the stationary point solution for quantum orbits p_q and the canonical momentum in the improved three-step model p_{ph} should be less than the size of the stationary point region: $|\Delta p| < |\partial^2 S/\partial p^2|^{-1/2} = (t_r - t_i)^{1/2}$. We can estimate $|\Delta p|$ as $|\Delta p| = |\Delta z/(t_r - t_i)|$, where $|\Delta z|$ includes the neglected imaginary displacement. This estimate yields $|\Delta z| < (t_r - t_i)^{1/2}$. Fig. 1.10 (left panel) illustrates this condition for typical experimental parameters (ω=0.057 a.u., I_p=15.6 eV, I=1.3 10^{14} W/cm^2): the improved three step model can not be applied for very short trajectories returning earlier than $\omega t_{r,ph} = 0.36$ or for harmonics lower than $N = 11$. Thus, for this particular set of parameters, all above threshold harmonics are within the applicability conditions of the improved three step model.

The right panel in Fig. 1.10 (right panel) compares the ionization times resulting from the Lewenstein model and the photoelectron model of HHG. The ionization times coincide for long trajectories. In these sense long trajectories indeed correspond to photoelectrons. The difference between the ionization times for short trajectories
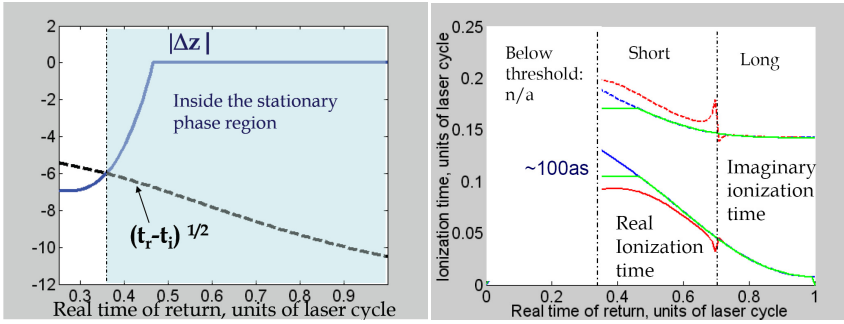
Figure 1.10 Left panel: Applicability region of the photoelectron model. Condition $|\Delta z| < (t_r - t_i)^{1/2}$ specifies the region of return times (filled), where the photoelectron model can be used. for $I_p =$15.6 eV, I=1.3 10^{14} W/cm^2, $\omega = 1.5$ eV. Right panel: real and imaginary ionization times for the Lewenstein model (red), photoelectron model with canonical momentum less than A_0 (green) and canonical momentum not limited by this condition (blue).

is associated with the presence of imaginary canonical momenta in the Lewenstein model. For the shortest trajectories the difference in real ionization times is about 100 asec for the chosen laser parameters: the ionization window is wider for the photoelectron model. As for the imaginary component of the ionization times, they are smaller in the photoelectron model. Therefore, short trajectories are less suppressed in this model than in the full Lewenstein model.

Mathematically, implementing the photoelectron model requires only one approximation - relaxing the return condition. Note that the requirement of perfect return to the origin is an *artefact* of neglecting the size of the ground state in the saddle point analysis. If we take into account the size of the ground state, than the return condition will naturally be relaxed: to be able to recombine, the electron has to return to the core within the size of the ground state. From this perspective, extension of the Lewenstein model to real systems including molecules should go hand in hand with relaxing the return condition for its real and part. The imaginary part of the electron displacement reflects the probability of trapping into bound states after tunneling. This probability is higher for short trajectories and leads to the respective decrease of the harmonic signal as $e^{\frac{F^2}{\omega^3}p_2^2(phi_r'' - phi_i'')}$ $((phi_r'' - phi_i'') < 0)$. The photoelectron model does not include trapping of the trajectories after ionization.

Measurement of ionization times might allow one to differentiate between these two models and pin down the nature of electron trajectories responsible for HHG.

1.8
HHG dipole for many electrons, including laser-induced dynamics in the ionic core between ionization and recombination

In multielectron systems, there are multiple ways of energy sharing between the liberated electron and the ion left behind. The ion can be left in its ground or one of excited electronic states. These options are referred to as different ionization channels. Multiple ionization channels lead to multiple HHG channels: the returning electron can recombine with the ion in its ground or one of the excited states.

Multiple HHG channels present different pathways connecting the same initial and final state - the ground state of the neutral system - via different electronic states of the ion. Thus, high harmonic emission in multielectron systems results from multichannel interference Smirnova et al (2009), i.e. the interference of harmonic light emitted in each channel. These interference naturally records multielectron dynamics excited upon ionization and probed by recombination Smirnova et al (2009). How important are these multiple channels? How hard is it to excite the ion upon strong field ionization?

Strong-field ionization is exponentially sensitive to the ionization potential I_p, suggesting that after ionization the molecular ion is typically left in its ground electronic state. In the Hartree-Fock picture, this corresponds to electron removal from the highest occupied molecular orbital (HOMO). However, multiple ionization channels can be very important in molecules due to the geometry of the molecular orbitals and the proximity of excited electronic states in the ion to the ground state.

The formalism described above in sections 1.1-1.7 is essentially a single-channel picture of HHG. It can be extended to multiple channels.

First, we introduce the Hamiltonian of an N-electron neutral molecule interacting with a laser field:

$$H^N = T_e^N + V_C^N + V_{ee}^N + V_L^N,$$

$$V_C^N = \sum_m \sum_{i=1}^{i=N} -\frac{Q_m}{|\mathbf{R}_m - \mathbf{r}_i|},$$

$$V_{ee}^N = \sum_{i \neq j}^{N} \frac{1}{|\mathbf{r}_i - \mathbf{r}_j|},$$

$$V_L^N = -\sum_i \mathbf{F}(t) \cdot \mathbf{d}_i = \sum_i \mathbf{F}(t) \cdot \mathbf{r}_i. \tag{1.71}$$

Here the nuclei are frozen at their equilibrium positions $\mathbf{R}_m$, the index m enumerates the nuclei with charges Q_m, the superscript N indicates the number of electrons involved, T_e^N is the electron kinetic energy operator, V_C^N describes the Coulomb potential of the nuclei, V_{ee}^N describes the electron-electron interaction, and V_L^N describes the interaction with the laser field. Hats on top of operators are omitted.

We will also use the Hamiltonian of the ion in the laser field H^{N-1} and the Hamiltonian of an electron H^e interacting with the laser field, the nuclei, and the $(N-1)$ electrons of the ion, $H^e = H^N - H^{N-1}$.

Populations of ionic states
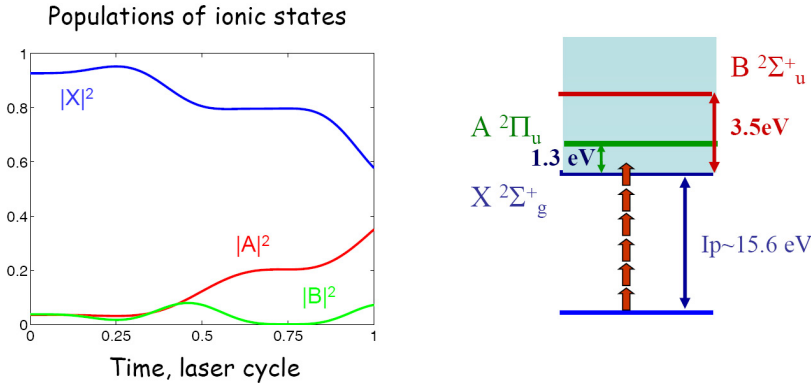
Figure 1.11 Left panel: Subcycle dynamics in the N_2^+ ion aligned at $\theta = 50^o$ to the laser field polarization: populations of the field-free ionic states X (blue), A (red), and B (green) in I=0.8 10^{14} W/cm^2, 800 nm laser field. Right panel: Electronic states of N_2^+ ion.

The Schroedinger equation for N-electron wave-function of the molecule, initially in its ground electronic state $\Psi_g^N(\mathbf{r})$, is

$$i\frac{\partial}{\partial t}\Psi^N(\mathbf{r},t) = H^N\Psi^N(\mathbf{r},t),$$
$$\Psi^N(\mathbf{r},t=0) = \Psi_g^N(\mathbf{r}) \tag{1.72}$$

Similar to the single-electron case, its exact solution can be written as

$$\Psi^N(\mathbf{r},t) = -i\int_0^t dt' U^N(t,t')V_L^N(t')U_0^N(t',0)\Psi_g^N(\mathbf{r}) + U_0^N(t,0)\Psi_g^N(\mathbf{r}). \tag{1.73}$$

Here U_0^N and U^N are the N-electron propagators. The former is determined by

$$i\partial U_0^N/\partial t = H_0^N U_0^N, \tag{1.74}$$
$$U^N(0,0) = 1. \tag{1.75}$$

where H_0^N is the field-free Hamiltonian of the molecule $H_0^N = H^N - V_L^N$. The latter is is a full propagator determined by $i\partial U^N/\partial t = H^N U^N$.

The harmonic dipole is

$$\mathbf{D}(t) = -i\langle U_0^N(t,0)\Psi_g(\mathbf{r})|\mathbf{d}|\int_0^t dt' U^N(t,t')V_L^N(t')U_0^N(t',0)\Psi_g^N(\mathbf{r})\rangle + c.c. \tag{1.76}$$

Just like in the one-electron case, propagation without the laser field is simple as long as the energy E_g and the wave-function of the initial state of a neutral molecule or an atom are known:

$$U_0^N(t,0)\Psi_g(\mathbf{r}) = e^{-iE_g t'}\Psi_g(\mathbf{r}), \tag{1.77}$$
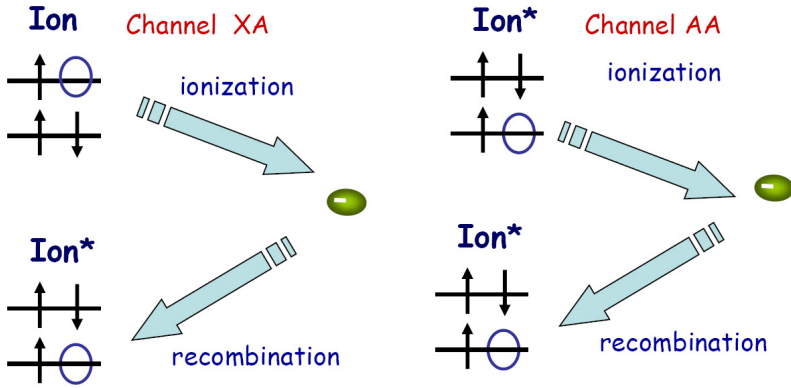
Figure 1.12 Left panel: Diagonal channel in HHG, associated with ionization from and recombination to the same orbital. Right panel: Cross-channel in HHG associated with ionization from and recombination to different orbitals. This channel is due to real excitations induced by the laser field between ionization and recombination.

Finding the full propagation $U^N(t, t')$ is just as hard as solving the multi-electron TDSE.

To simplify the analysis, we will make the following two approximations. First, we shall neglect correlations between the electrons in the ion and the liberated electron after ionization. In this case the full propagator factorizes into two independent parts describing the evolution of the continuum electron and the evolution of the ion in the laser field between ionization and recombination: $U^N(t, t') \simeq U^{N-1}(t, t')U^e(t, t')$. Second, we will keep the analysis at the level of the SFA for the continuum electron, just like we did in the single electron case considered above: $U^e(t, t') \simeq U^e_V(t, t')$.

One can improve upon these two approximations by including the electron-electron correlations during ionization perturbatively Walters and Smirnova (2010) and by using the eikonal-Volkov states Smirnova and Ivanov (2008) for the continuum electron, instead of the plane wave Volkov states. The eikonal-Volkov states include the laser field fully, the interaction of the continuum electron with the core in the eikonal approximation, and also take into account the interplay between these two interactions (the so-called Coulomb-laser coupling, Smirnova et al (2007)). Moreover, if we can factorize the dipole response into the usual steps – ionization, propagation, recombination, we can think of improving each of the three steps separately, e.g. by using improved ionization and recombination amplitudes that include the electron-electron correlation beyond the perturbation theory.

Just like in the one-electron formalism considered above, we will introduce identity resolved on the momentum states of continuum electron, but now we also have to

include the electronic states of the ion [5]

$$I = \int d\mathbf{k} \sum_n \mathbb{A} |n^{(N-1)} \otimes \mathbf{p}_t^n\rangle \langle n^{(N-1)} \otimes \mathbf{p}_t^n| \mathbb{A}, \qquad (1.78)$$

The harmonic dipole becomes

$$\mathbf{D}(t) = -i \int_0^t dt' \int d\mathbf{p} e^{iE_g(t-t')} \langle \Psi_g^N | \mathbf{d} | U^{N-1}(t,t') | n^{(N-1)} \rangle U_V^e(t,t') | \mathbf{p}_t \rangle$$
$$\times \langle p_t^n n^{(N-1)} | V_L^N(t') | \Psi_g^N \rangle + cc. \qquad (1.79)$$

Note a crucial change compared to the single-channel case: the appearance of the laser-induced dynamics between the bound states of the ion, described by the propagator $U^{N-1}(t,t')|n^{(N-1)}\rangle$. This dynamics can be calculated if the dipole couplings d_{nm} between all essential states, as well as their eigen-energies E_m, are known.

Consider, for example, the case of an N_2 molecule with three essential states in the N_2^+ ion, denoted as X, A and B, see Fig.1.11. The time-dependent transition amplitudes $a_{mn}(t,t')$ between the state n populated at the moment t' and the state m at the moment t are given by $a_{mn}(t,t') = \langle m^{(N-1)} | U^{N-1}(t,t') | n^{(N-1)} \rangle$. It is a solution of the equation:

$$\frac{d\mathbb{A}_n}{dt} = [\mathbb{H} + \mathbb{V}(t)] \mathbb{A}_n, \qquad (1.80)$$

where for our three ionic states the Hamiltonian of the ion is $\mathbb{H} = \begin{bmatrix} E_1 & 0 & 0 \\ 0 & E_2 & 0 \\ 0 & 0 & E_3 \end{bmatrix}$,

with E_n the energies of the three states. Interaction between these three states is described by the matrix of the laser-induced couplings, $V_{nm}(t) = -\mathbf{d}_{nm} \cdot \mathbf{F}(t)$,

$\mathbb{V}(t) = \begin{bmatrix} 0 & V_{12} & V_{13} \\ V_{21} & 0 & V_{23} \\ V_{31} & V_{32} & 0 \end{bmatrix}$. Finally, $\mathbb{A}_n = \begin{bmatrix} a_{1n}(t,t') \\ a_{2n}(t,t') \\ a_{3n}(t,t') \end{bmatrix}$ is the vector describing the population amplitudes of all essential ionic states, starting from the state n at time t'.

Let us introduce channel specific Dyson orbitals $\Psi_n^D(\mathbf{r}) \equiv \langle n^{(N-1)} | \Psi_g^N(\mathbf{r}) \rangle$. These are the overlaps between the N-electron wavefunction of the ground state of the neutral and the $N-1$ electron wavefunction of the ionic state $|n\rangle$. Let us assume that the dipole operator that starts ionization at the moment t' in Eq.(1.79) acts only on the ionized electron. In this case the multielectron dipole D_{mn}, which corresponds to leaving the ion in the state n after ionization and then recombination with the ion in the state m, can be re-written in the form very similar to the one-electron

---

5) Here we use the field-free states of the ion. Note that the ion is polarized by the laser field when it is created in the strong laser field. Thus, to set up an initial condition in the ion upon ionization, one should first find the polarized ionic states, also called the quasi-static states, which include the electric field of the laser in the quasi-static approximation. Then one should project these states on the field-free basis.

case:

$$\mathbf{D}_{mn}(t) = i \int_0^t dt' \int d\mathbf{p} \mathbf{d}_m^*(\mathbf{p} + A(t)) a_{mn}(t, t') e^{-iS(\mathbf{p}, t, t')} \mathbf{F}(t') \mathbf{d}_n(\mathbf{p} + A(t')),$$

$$\mathbf{d}_n(\mathbf{p} + A(t)) = \langle \mathbf{p} + \mathbf{A}(t) | \mathbf{d} | \Psi_n^D \rangle,$$

$$S(\mathbf{p}, t, t') = \frac{1}{2} \int_{t'}^t (\mathbf{p} + \mathbf{A}(\tau))^2 d\tau + I_p(t - t'). \tag{1.81}$$

The total harmonic signal results from coherent superposition of the dipoles D_{mn} associated with each ionization-recombination channel:

$$D(t) = \sum_{m,n} D_{mn}(t). \tag{1.82}$$

Substantial sub-cycle transitions, such as those seen in Fig.1.11 for the N_2^+ ion in typical experimental conditions, have crucial impact on harmonic radiation. They lead to the appearance of the cross-channels in HHG (off-diagonal channels D_{mn} in equation (1.82)) since the state of the ion changes between the ionization and recombination, see Fig.1.12. These channels are indeed substantial in high harmonic generation from the N_2 molecules Mairesse et al (2010), as illustrated in Fig.1.11.

In recent literature on high harmonic generation one can often come across a rather loose language, which refers to different ionization and recombination channels as associated with different Hartree-Fock molecular orbitals. This language should not be taken literally as the statement of the applicability of the Hartree-Fock picture and of the physical reality of the Hartree-Fock orbitals as observable physical quantities. Loosely speaking, removing an electron from the highest occupied molecular orbital (HOMO) creates the ion in the ground state. Removing electron from one of the lower lying orbitals (e.g. HOMO-1, HOMO-2) creates the ion in one of excited states. Thus, reference to orbitals should only be understood as a language for describing ionization and recombination channels associated with different multi-electron states of the ion – and those are physically relevant and observable. In the orbital language, electron removal from an orbital creates a hole in this orbital. The laser induced dynamics in the ion, moves the hole between the orbitals in the time window between ionization and recombination, see Fig.1.12.

Application of the saddle point method in each channel leads to the following half-cycle dipole for the given ionization – recombination channel:

$$D_{mn}^j(t) = a_{rec}^m(\mathbf{p}_s, t) a_{prop}^{mn}(t, t_i) a_{ion}^n(\mathbf{p}_s, t_i), \tag{1.83}$$

$$a_{ion}^n(\mathbf{p}_s, t_i) = \left[\frac{2\pi}{S_{t_i, t_i}''} \right]^{1/2} e^{-iS(\mathbf{p}_s, t_i', t_i)} \mathbf{F}(t_i) \mathbf{d}_n(\mathbf{p}_s + A(t_i)), \tag{1.84}$$

$$a_{prop}^{mn}(t, t_i) = \frac{(2\pi)^{3/2}}{(t - t_i)^{3/2}} e^{-iS(\mathbf{p}_s, t, t_i')} a_{mn}(t), \tag{1.85}$$

$$a_{rec}^m = \mathbf{d}_m^*(\mathbf{p}_s + \mathbf{A}(t)). \tag{1.86}$$

Here we have considered the harmonic dipole on the real time axis. Note that the propagation amplitude is modified to include the laser –induced dynamics in the ion

$a_{mn}(t)$. The full dipole for each ionization-recombination channel obtains as the sum over different half-cycles and the harmonic spectrum results from the FFT of the full dipole $d_{mn}(N\omega)$:

$$d_{mn}(t) = \sum_j D_{mn}^j(t), \tag{1.87}$$

$$d_{mn}(N\omega) = \int dt d_{mn}(t) e^{iN\omega t}. \tag{1.88}$$

The complete harmonic response obtains by adding coherently the contributions of all ionization – recombination channels.

1.9
Outlook

Having factorized the dipole, we can use improved amplitudes for each step. This is the key components of the current theoretical work in high harmonic spectroscopy from molecules.

Improving ionization. Improved ionization amplitude can be taken from the semi-analytical and/or numerical approaches. For example, one can use the results of Murray (2011), where the ionization amplitude is represented as:

$$\widetilde{a}_{ion}^n(\mathbf{p}s, t_i) = \mathbb{R}_{\mathfrak{lm}}(I_p, F) e^{-iS(\mathbf{p}_s, t_i', t_i)}. \tag{1.89}$$

The exponent describes the sub-cycle dynamics of strong-field ionization, i.e. is the same as for the atomic case and a short-range potential. The pre-factor $\mathbb{R}_{\mathfrak{lm}}(I_p, F)$ accounts for the influence of the core potential and the shape of the initial state on the ionization rate. For atoms, this pre-factor has been derived in the seminal papers of Perelomov, Popov and Terent'ev (see Perelomov and Terent'ev (1966, 1967); Perelomov and Popov (1967); Popov and Perelomov (1968)). A simple recipe for incorporating their results into the sub-cycle ionization amplitudes can be found in Yudin and Ivanov (2001). For molecules, the pre-factor is discussed in Murray (2011).

Improving propagation. In addition to the dynamics in the molecular ion, including the laser-induced transitions between different ionic states, the second most important modification of the propagation amplitudes is the incorporation of the possible transverse nodal structure in the continuum wavepackets. The nodal planes in the continuum wavepacket arise during tunnelling from bound states. For example, in a CO_2 molecule, the HOMO and the corresponding Dyson orbital have nodal planes parallel and perpendicular to the molecular axis. Consequently, in the case of tunnel ionization with molecular axis aligned parallel to the polarization of the ionizing field, the nodal plane will not only reduce the ionization rate, but will also be imprinted on the shape of the electronic wavepacket that emerges after ionization. Propagation between ionization and recombination will lead to spreading of the wavepacket, but it will not remove the presence of the node as the wavepacket returns to the core. Clearly, this aspect of propagation is important for the recombination amplitude.

Consider, for example, ionization from a state with angular momentum $L = 1$. Its projection on the laser polarization is either $L_z = 0$ (no nodal plane along the electric field) or $L_z = 1$ (nodal plane along the electric field). After tunnelling, in the plane orthogonal to laser polarization, in the momentum space the continuum wavepackets are (see Murray and Yu. (2010)):

$$\Psi_{L_z=0}(p_\perp) \propto e^{-\frac{p_\perp^2}{2}\tau}$$

$$\Psi_{L_z=1}(p_\perp) \propto \frac{p_\perp}{\kappa} e^{i\phi_p} e^{-\frac{p_\perp^2}{2}\tau} \tag{1.90}$$

where $\tau = \text{Im}\, t_i$ and $\kappa = \sqrt{2I_p}$, and ϕ_p is the angle between $p_\perp$ and the x-axis. As we can see, the presence of the nodal plane for $L_z = 1$ leads to additional term $p_\perp/\kappa$. We now propagate these wavepackets until the recombination time t_r. Fourier transforming back into the coordinate space, in the plane orthogonal to laser polarization we get

$$\Psi_{L_z=0}(\rho) \propto e^{-\frac{\rho^2}{2(t_r-t_i)}}$$

$$\Psi_{L_z=1}(\rho) \propto \frac{\rho}{\kappa(t_r-t_i)} e^{i\phi} e^{-\frac{\rho^2}{2(t_r-t_i)}} \tag{1.91}$$

where ρ is the transverse radial coordinate, and ϕ is the angle between the radial vector and the x-axis. Recalling that $x = \rho\cos\phi$, we see that if we combine the $L_z = \pm 1$ states to form the real-valued spherical harmonic p_x, the presence of the nodal plane effectively changes the dipole operator $\mathbf{d}$ to $\mathbf{d} \cdot x/(\kappa(t_r - t_i))$.

In most experiments with molecular HHG to-date, the alignment distribution is rather broad. Even if the molecular ensemble is, on average, aligned parallel to the laser polarization, for most molecules the characteristic alignment angle would be sufficiently different from that associated with the nodal plane. In this case, the relative importance of the nodal planes in recombination is reduced. However, for well-aligned molecular ensembles this would become a significant factor.

Improving recombination. The recombination step can be significantly improved beyond the SFA, if one uses the recombination dipoles $d_m^*(\mathbf{p}_s + A(t))$ calculated using ab-initio approaches. For example, the quantitative rescattering theory (see Lin et al (2010)) relies on using Schwinger variational method to calculate field-free recombination matrix elements. Alternatively, one can use the R-matrix approach. Both allow one to incorporate the full complexity of the recombination process, including the channel coupling due to the electron-electron correlation. The drawback of these methods, at the moment, is the absence of the laser field in the calculations of the recombination amplitudes. RefsSmirnova et al (2009) use the eikonal approximation for continuum states to obtain improved dipoles in the single-channel approximation, which dresses the continuum electron with the laser field, but the core potential is only included in the eikonal approximation, and the correlation-induced channel coupling is neglected. Improving recombination amplitudes to account for all effects – channel coupling due to electron-electron correlation, core potential, and the laser field, is one of the key theory challenges today.

With each of the three steps in the harmonic response is improved, the original SFA-based theory turns from purely qualitative into quantitative. Separation of three steps, crucial for our ability to improve each of them separately, benefits from high intensity of the driving field and large oscillation amplitude of the active electron. High field intensity also lies at the heart of the main difficulties in building adequate theoretical description. Nevertheless, the effort is worth the investment: the combination of attosecond temporal and angstrom spatial resolution is extremely valuable. High harmonic spectroscopy appears to be well suited for tracking the multi-electron dynamics induced by the ionization process.

It is very attractive to replace the ionization step induced by the IR field with the one-photon ionization absorption by a controlled asec XUV pulse, phase-locked to the strong IR field. The latter that would drive the continuum electron. Such arrangement should allow one to move from dealing with outer valence electrons to dealing with inner valence and deeper lying electrons. This appears to be an exciting regime for tracking the hole dynamics initiated by inner-valence or deeper ionization. Importantly, for the deeply bound orbitals, the effect of the IR driving field on the core-rearrangement and the hole dynamics should be substantially less than for the outer-valence electrons.

1.10
Appendix A: Saddle point method

Saddle point method is one of the key techniques in the analytical strong field theory. It is an asymptotic method, which allows one to analytically evaluate the integrals from highly oscillating functions, such as e.g. the integral in equation (1.20).

1.10.1
Integrals on real axis

How would one calculate the following integral,

$$I = \int_a^b f(x)e^{\lambda h(x)}dx \tag{1.92}$$

for some smooth functions $f(x)$ and $h(x)$, without knowing much about them, or if they look ugly and complicated? All we know is that they are real-valued functions on the real axis x.

In general, one would think that there isn't much one can do. Fortunately, this is not the case if positive real λ is large, $\lambda \gg 1$ – then, the integral can be calculated.

1.10.1.1 **Contribution of end points**
The first idea that comes to my mind when looking at an integral is to try integration by parts. Here, it works just fine under certain circumstances, see later. The first stumbling block meets you right at the gate: how does one integrate by parts if both $h(x)$ and $f(x)$ are unknown?

The trick is simple:

$$
\begin{aligned}
I &= \int_a^b f(x)e^{\lambda h(x)}dx \\
&= \int_a^b dx \frac{f(x)}{\lambda h'(x)}\lambda h'(x)e^{\lambda h(x)} = \\
&= \frac{1}{\lambda}\frac{f(x)}{h'(x)}e^{\lambda h(x)}|_a^b - \frac{1}{\lambda}\int_a^b dx e^{\lambda h(x)}\left[\frac{d}{dx}\frac{f(x)}{h'(x)}\right]
\end{aligned}
\tag{1.93}
$$

We have started with the integral that did not have a small parameter $1/\lambda$ in front. We now have two terms: the first comes from the contributions at the end points. The second term is another integral, now with a small parameter in front. Dealing with it in the same way as with the original integral, we will get terms proportional to $1/\lambda^2$ and so on.

Thus, we conclude that the main contribution to the integral comes from the end points, and is given by the first term:

$$
\begin{aligned}
I &= \int_a^b f(x)e^{\lambda h(x)}dx = \\
&= \frac{1}{\lambda}\left[\frac{f(b)}{h'(b)}e^{\lambda h(b)} - \frac{f(a)}{h'(a)}e^{\lambda h(a)}\right] + O(\lambda^{-2})
\end{aligned}
\tag{1.94}
$$

This result is applicable unless there is a problem with the second term in Eq.(1.93) – the integral

$$
-\frac{1}{\lambda}\int_a^b dx e^{\lambda h(x)}\frac{d}{dx}\frac{f(x)}{h'(x)}
\tag{1.95}
$$

The problem arises if $h'(x) = 0$ somewhere between the two end points of the integral. What do we do then? Obviously, the hint is that the points where $[f(x)/h'(x)]$ diverges can bring major contributions to the integral.

Given that $\lambda \gg 1$, the way the exponential function changes between a and b is most important. The first possibility is $h' \neq 0$ in the integration interval. Then, the integral is accumulated at the end points, and the end point where $h(x)$ is larger dominates. In general, for an exponential function $e^{\lambda h(x)}$ the main contribution to the integral will come from the region where it reaches its maximum value – and hence where $h'(x) = 0$.

Suppose that somewhere between a and b the derivative $h' = 0$. If the function $h(x)$ has a minimum, the contribution of this minimum won't be competitive with the contributions from the end points (remember that λ is large and positive). But if it has a maximum, then the main contribution to the integral comes from the region near the maximum. The way to handle this situation is described in the next section.

1.10.1.2 **The Laplace Method**

Let us consider an integral from a function $f(x)$ shown in Fig.1. The function is bell-shaped, has a maximum at the point x_0, where its first derivative is, of course, equal to zero, and quickly falls off to each side of x_0.
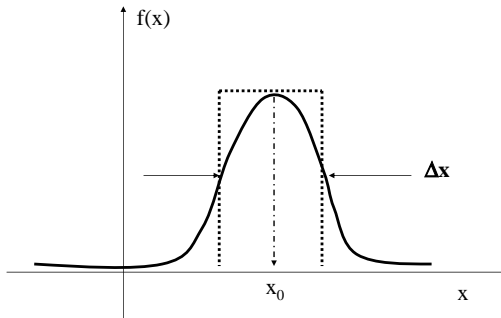
Figure 1.13 Integral from a bell-shaped curve

The idea of calculating this integral is very simple - all we need is to find the effective width Δx of the bell-shaped curve, and then the integral is

$$I = \int_{-\infty}^{\infty} f(x)dx = f(x_0)\Delta x \tag{1.96}$$

Let us first try some simple estimates of the width Δx. In order to do it, we expand $f(x)$ around x_0 in Taylor series, remembering that the first derivative is zero at this point:

$$\begin{aligned}
f(x) &\approx f(x_0) + \frac{1}{2}f''(x_0)(x - x_0)^2 \\
&= f(x_0) - \frac{1}{2}|f''(x_0)|(x - x_0)^2
\end{aligned} \tag{1.97}$$

Notice that I have explicitly used the fact that the second derivative at the local maximum is negative.

A potential candidate for the width Δx is the full width at half maximum (FWHM). Half-width $\Delta x/2$ at each side is given by

$$f(x_0) - \frac{1}{2}|f''(x_0)|(\Delta x/2)^2 = f(x_0)/2, \tag{1.98}$$

This gives us $\Delta x = \sqrt{4f_0/|f''|}$.

More accurate calculation of the required width comes from the following trick, which will also smoothly bring us into the saddle point method

$$I = \int f(x)dx = \int e^{\ln f(x)}dx \tag{1.99}$$

This innocent at first glance transformation allows us to reduce the integral to a familiar Gaussian form. We proceed by expanding $\ln f(x)$ in the Taylor series, remembering that $f'(x_0) = 0$ and $f''(x_0) = -|f''(x_0)|$:

$$I = \int e^{\ln f(x)} dx \simeq \int e^{\ln f(x_0) - \frac{|f''(x_0)|}{f(x_0)} \frac{(x-x_0)^2}{2}} \tag{1.100}$$

Recalling that the integral from a Gaussian is

$$\int_{-\infty}^{\infty} e^{-ax^2} = \sqrt{\pi/a} \tag{1.101}$$

and setting the limits of our integral to $\pm\infty$, we get the final answer

$$I = f(x_0)\sqrt{2\pi f(x_0)/|f''(x_0)|} \tag{1.102}$$

As you can see, the width Δx turned out to be pretty close to FWHM.

1.10.1.3 **Saddle point method: the steepest descent in a complex plane**

We now move to the *saddle point method* which is used for integrals of complex-valued functions:

$$I = \int_C e^{\lambda f(z)} dz \tag{1.103}$$

where λ is large and positive, and the rest is hidden in $f(z)$. The integral is to be done over a contour C, and the only good thing about this contour is that its ends, somewhere far away from the place of action, do not contribute to the value of the integral.

There assumed to be no poles, so that we are allowed to deform the contour C as we wish. The key of the steepest descent is a clever modification of the integration contour.

First, note that a complex function $f(z)$ has real and imaginary parts, $f(z) = u(z) + iv(z) \equiv u(x, y) + iv(x, y)$ where x and y are the real and the imaginary parts of z, $z = x + iy$.

Let us now look at the integral more closely and recall the previous section, where the integration was based on expanding the function around a maximum and reducing the integrand to a Gaussian. In our case we have a function $\exp(\lambda u + i\lambda v)$ that both changes very rapidly in absolute value due to the λu part and also oscillates like crazy due to the λv part. The trick of the steepest descent is to modify the contour of integration in such a way that it will go through a place where the real part u climbs to a maximum along the contour and then quickly falls, while the imaginary part v stays constant along the same contour, freezing any fast oscillations.

It may not be obvious at first glance that such modification of the contour is possible. But it is.

We start in a manner entirely analogous to the previous section. Let us assume that the function $f(z)$ has zero derivative at the point $z_0 = x_0, y_0$, where x_0 and y_0 are

coordinates in complex plane; the point z_0 lies somewhere between the left and the right ends of the contour C.

If $f_z(z_0) = 0$, then both the real and the imaginary parts of f must have zero derivatives there:

$$u_x = v_x = 0, \quad v_y = u_y = 0 \tag{1.104}$$

Thus, not only at z_0 the absolute magnitude of our function goes through an extremum, but also the oscillating part is stationary. Another important observation is that the gradients of the two functions, ∇u and ∇v, are always orthogonal to each other:

$$\nabla v \cdot \nabla u = u_x v_x + u_y v_y = 0 \tag{1.105}$$

This is the consequence of the Cauchy-Riemann conditions:

$$u_x = v_y \quad v_x = -u_y \tag{1.106}$$

Gradient is the direction along which the function changes. If we move along the gradient of u, following the path of its steepest rise and fall through the point z_0, we are also moving orthogonal to the gradient of v. Thus, v will stay constant, and fast oscillations are frozen. We see that the desired modification of the contour is indeed possible.

How should the landscape of $u(x, y)$ look like? Due to the same Cauchy-Riemann conditions the functions u and v can only have *saddle points* at z_0:

$$u_{xx} + u_{yy} = 0 \quad v_{xx} + v_{yy} = 0 \tag{1.107}$$

Real mountain peaks, which go down in all directions, only happen at singularities, and we decided that there would be no singularities in $f(z)$.

Therefore, the landscape of the function u around the point z_0 must look something like shown in Fig.2

All we have to do now is to find the correct path of the *steepest descent through the saddle point*, such that u will rise as quickly as possible as we approach the saddle point and then decrease as quickly as possible as we leave the saddle point. The Cauchy-Riemann conditions promise us that, while we are at it, v will stay constant.

Let us expand $f(z)$ in Taylor series around z_0, remembering that $f'(z_0) = 0$:

$$f(z) \approx f(z_0) + \frac{1}{2} f''(z_0)(z - z_0)^2 \tag{1.108}$$

Of course, $f''(z_0)$ is a complex number, which we will denote as $f''(z_0) = \alpha \exp(i\theta)$. If our path through the saddle point goes at some angle ϕ, then $z - z_0 = \rho \exp(i\phi)$ and

$$\frac{1}{2} f''(z_0)(z - z_0)^2 = \frac{1}{2} \alpha \rho^2 e^{i(\theta + 2\phi)} \tag{1.109}$$

Now, the simple trick is to choose the angle ϕ properly – we set

$$e^{i(\theta + 2\phi)} = -1 \tag{1.110}$$
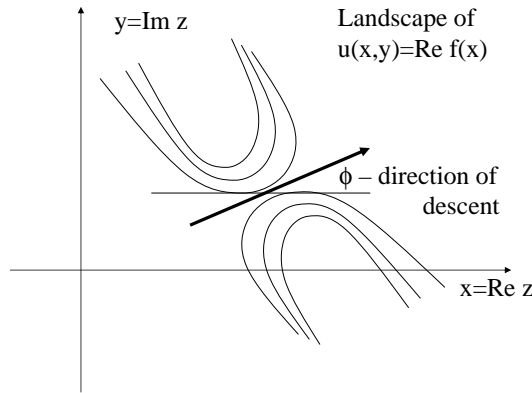
Figure 1.14 Saddle point method. The landscape of $u(x, y) = \operatorname{Re} f(z)$ around the point z_0 where $f' = 0$

and keep the angle ϕ given by the above condition fixed, changing only ρ, so that $dz = d(z - z_0) = \exp(i\phi)d\rho$.

If we do this, the integral along such path will look as

$$I = e^{\lambda f(z_0)} e^{i\phi} \int_{C'} e^{-\lambda \alpha \frac{\rho^2}{2}} d\rho \tag{1.111}$$

where the deformed contour C' is going through the saddle point as a straight line at an angle ϕ. Note that indeed there are no oscillations along such path, and the real integrand decays as Gaussian.

The limits of integration are now extended to plus-minus infinity and the integral is done,

$$I = e^{\lambda f(z_0)} e^{i\phi} \sqrt{\frac{2\pi}{\lambda \alpha}} \tag{1.112}$$

Recall that $\alpha \equiv |f''(z_0)|$.

At this point we are almost done, but three important remarks are still in order.

First, there is ambiguity in the definition of the direction ϕ from $\exp(i(\theta + 2\phi)) = -1$. Indeed, the total angle $\theta + 2\phi$ could be both plus and minus π. Thus, formally, without looking at the landscape shown in Fig.2, we have a choice of two ϕ:

$$\phi_1 = -\theta/2 + \pi/2; \quad \phi_2 = -\theta/2 - \pi/2 \tag{1.113}$$

The whole idea of the method is to choose such direction that you never have to cross the 'mountains' in the landscapes of $u(x, y)$ and $v(x, y)$. You should choose the

direction (deforming the contour C) that takes you from the valley, through the saddle point, into another valley. Otherwise, you will also have to include the contributions of the 'mountains' into the integral. Usually, it is the first choice that works, but one should take a look at the landscape and check. The wrong option will go an obvious wrong way, crossing into the tops of the mountains rather than staying all the way in the valley smoothly climbing to the saddle. We shall see the example of it in the next section.

Second, if there are several saddle points - i.e. $f(z)$ has many points where its derivative is zero, the integral will be the sum of contributions from all these points. Then individual phases ϕ for each saddle point become very important.

Third, there is a modification of the prefactor when dealing with multidimensional integrals:

$$I = \int_C e^{\lambda f(z)} dz, \tag{1.114}$$

$$I \simeq \left(\frac{2\pi}{\lambda}\right)^{n/2} e^{\lambda f(z_0)} \frac{1}{\sqrt{-f_{zz}(z_0)}}, \tag{1.115}$$

where f_{zz} is Hessian matrix (the matrix of second derivatives of the function f).

1.10.2
Stationary phase method

The stationary phase method is a simple application of the saddle point to a function which has a purely imaginary phase:

$$I = \int g(x) e^{i\lambda f(x)} dx \tag{1.116}$$

where $g(x)$ is a benign, very slowly changing function which does not do much - just makes sure that the integrand goes to zero at infinity. The constant λ is again real and positive, the integral is supposed to be performed along the real axis and the function $f(x)$ is purely real on the real axis. Intuitively, it is clear that if the function $\exp(i\lambda f(x))$ is oscillating very quickly, its integral averages to zero unless there are some points where the oscillations freeze. These areas are the regions where the phase of the oscillation, $f(x)$, stays nearly constant, i.e. areas around the point where the derivative turns to zero, $f' = 0$, see Fig. 3.

Well, the problem can be immediately turned into that studied in the previous section. Again, suppose that the derivative $f' = 0$ at some point x_0. We use the same Taylor expansion around this point and denote $x - x_0$ as, say, ξ. The integral is approximated as

$$I = g(x_0) e^{i\lambda f(x_0)} \int e^{i\lambda f''(x_0) \frac{\xi^2}{2}} d\xi \tag{1.117}$$

and we will assume that $f'' = \alpha > 0$ (f is a real-valued function and x_0 is on the real axis, hence f'' is real). The case $f'' < 0$ is handled in an identical manner.

f(x)

stationary
phase point

x_0

x
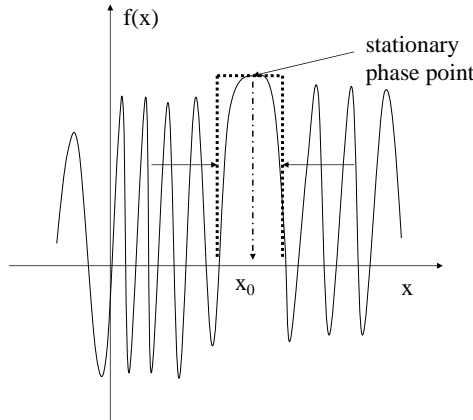
Figure 1.15 Stationary phase method. The integral comes from the area where the integrand does not oscillate as much.

Calculation of the integral

$$\int e^{i\lambda\alpha\frac{\xi^2}{2}}\,d\xi \tag{1.118}$$

follows the exact prescription of the saddle point method. Obviously, the phase θ of the second derivative (see previous section) is $\theta = \pi/2$ (i.e. $i\alpha = \alpha\exp(i\pi/2)$) and the contour of integration has to be turned at an angle ϕ to the real axis such that $\theta + 2\phi = \pm\pi$. This yields the two possible choices of ϕ: $\phi = +\pi/4$ and $\phi = -3\pi/4$; the answer for the integral is

$$I = g(x_0)e^{i\lambda f(x_0)}\sqrt{\frac{2\pi}{\alpha\lambda}}e^{i\phi} \tag{1.119}$$

To find the correct choice of ϕ one has to look at the landscape of $u(x,y) = \mathrm{Re}\,iz^2 = -2xy$. The landscape is shown in Fig.4. The correct choice is obviously the first one, $\phi = +\pi/4$, the second would mean that the contour has to be deformed as shown in Fig.4 with a dashed line, going through high mountains on the way to the saddle to cross it in the opposite direction of $\phi = -3\pi/4$.

So, the final answer is

$$I = g(x_0)e^{i\lambda f(x_0)}\sqrt{\frac{2\pi}{\alpha\lambda}}e^{i\pi/4} \tag{1.120}$$

y=Im z

Landscape of
u(x,y)=Re iz²= -2xy

$\phi=\pi/4$ - correct
direction of descent

x=Re z

$\phi=-3\pi/4$ - wrong
direction of descent
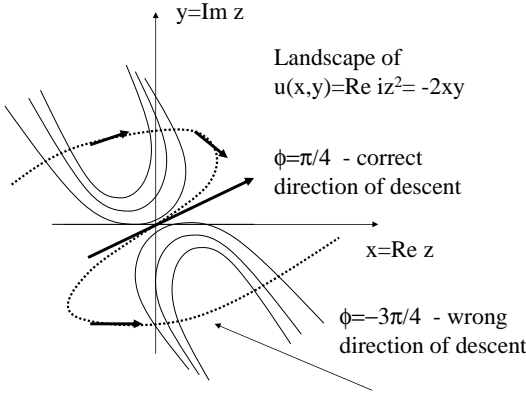
Figure 1.16 Stationary phase method. Correct and incorrect paths of the steepest descent
for $f(z) = iz^2$.

1.11
Appendix B: Treating the cut-off region: regularization of the divergent stationary phase solutions

In this subsection we briefly outline the idea of so-called uniform approximation - one of the approaches handling the merging stationary points. The regularization involves the following two steps. First we need to find a specific real return time $t_r = t_{r0}$ and associated $t_i = t_{i0}$, $p_s = p_{s0}$, such that $\partial^2 S(t_{r0}, t_{i0}, p_{s0})/\partial t^2 = 0$. In practice one can simply pick the real return time corresponding to the cut-off energy. The next step requires expanding the total action in equation (1.22) around $t = t_{r0}$ in Taylor series up to the third order:

$$S(t, t_{i0}, p_{s0}) = S(t_{r0}) + (t - t_{r0})S'_{tt} + \frac{(t - t_{r0})^2}{2}S''_{tt} + \frac{(t - t_{r0})^3}{6}S'''_{ttt}, \quad (1.121)$$

where all the derivatives of $S(t, t_{i0}, p_{s0})$ are taken at t_{r0}. Finally, substituting expansion (1.121) to the harmonic dipole

$$D(N\omega) \propto \int_{-\infty}^{\infty} dt e^{iN\omega t} e^{-iS(t, t_{i0}, p_{s0}) + iN\omega t} + c.c. \quad (1.122)$$

and using Airy function

$$\int_{-\infty}^{\infty} dt \cos(at^3 \pm xt) \equiv \frac{\pi}{(3a)^{1/3}} Ai \left[\frac{\pm x}{(3a)^{1/3}} \right]. \quad (1.123)$$

Now we introduce the "cut-off harmonic number" N_0 and the distance from cut-off: $N = N - N_0$:

$$N_0\omega = E_{rec}(t_{r0}) + I_p, \tag{1.124}$$

here $E_{rec}(t_{r0}) = p_{s0} + A(t_{r0})$ is the recollision energy at time t_{r0} and N_0 does not have to be integer. The dipole near cut-off is expressed via Airy function:

$$\int_{-\infty}^{\infty} dt e^{iN\omega t} e^{-iS(t,t_{i0},p_{s0})+iN\omega t} + c.c. = \int_{-\infty}^{\infty} d\xi \cos(\frac{\chi}{6}\xi^3 \pm \Delta N\omega\xi). \tag{1.125}$$

$$D(N\omega) \propto \frac{2\pi}{(\chi/2)^{1/3}} Ai\left[\frac{\Delta N\omega}{(\chi/2)^{1/3}}\right], \tag{1.126}$$

where $\chi \equiv -S'''_{ttt}(t_{r0})$ and can be estimated as $\chi \cong v(t_{r0})F_0\omega$, given that $F'_t(\chi) \cong F_0\omega$ and $F(\chi) \cong 0$. Using the asymptotic expansion of Airy functions we obtain simple expressions for the dipole just before and after the cut-off. Before (for $\Delta N < 0$) the cut-off of harmonic spectra the dipole oscillates: $Ai \sim \cos(-(\Delta N\omega)^{3/2}(\frac{8}{9\chi})^{1/2})$, after the cut-off the harmonic dipole exponentially decreases $Ai \sim e^{-(\Delta N\omega)^{3/2}(\frac{8}{9\chi})^{1/2}}$. The oscillations of harmonic dipole before the cut-off are due to the interference of short and long trajectories.

1.12
Appendix C: Finding saddle points for the Lewenstein model

In section 1.5 we have described how one can find all saddle point solutions in the Lewenstein model for fixed harmonic number N. Here we present an alternative and equivalent approach of finding the saddle point solutions, i.e. solving equations Eq. (1.34,1.35,1.36), which can be used in all cases, but is particulary convenient if the Fourier transformation is performed numerically. The idea is to solve Eqs. (1.34,1.35,1.36) "forward", i.e. fix the grid of real recombination times and find all the other saddle point solutions and the corresponding harmonic number N. The recombination condition Eq. (1.36) ($p_{s,\parallel} = p' + ip''$) can be re-written as follows:

$$\left(\Delta p' + i\Delta p''\right)^2 = 2(N\omega - I_p), \tag{1.127}$$

$$\Delta p' \equiv p' - A_0 \sin(\phi'_r)\cosh(\phi''_r), \tag{1.128}$$

$$\Delta p'' \equiv p'' - A_0 \sinh(\phi''_r)\cos(\phi'_r). \tag{1.129}$$

yielding

$$\left(\Delta p'\right)^2 - \left(\Delta p''\right)^2 + 2i\Delta p'\Delta p'' = 2(N\omega - I_p). \tag{1.130}$$

Since the right hand side of this equation is real, we obtain that $\Delta p'\Delta p'' = 0$. For above threshold harmonics $(N\omega - I_p) > 0$ and $\Delta p' \neq 0$, $\Delta p'' = 0$. For below threshold harmonics $(N\omega - I_p) < 0$ and $\Delta p' = 0$, $\Delta p'' \neq 0$. Separating imaginary and real parts in Eqs. (1.34,1.35) we obtain four equations quoted in the main text

(see Eqs.1.41,1.42,1.45,1.46). Supplementing these equations for above threshold harmonics by $\Delta p'' = 0$ yielding

$$p_2 = \sinh(\phi_r'') \cos(\phi_r'),\tag{1.131}$$

and for below threshold harmonics by $\Delta p' = 0$ yielding

$$p_1 = \sin(\phi_r') \cosh(\phi_r''),\tag{1.132}$$

we obtain five equations.

For above threshold harmonics for each fixed ϕ_r' we use equations (1.45,1.46) to express ϕ_i', ϕ_i'' via p_2 and p_1 and then we use Eq.(1.131) to exclude p_2 and substitute $\phi_i'(p_1, \phi_r'')$, $\phi_i''(p_1, \phi_r'')$ and $p_2(p_1, \phi_r'')$ into equations Eqs.(1.41,1.42). Using gradient method we can now find the minima of the function $F = F_1^2 + F_2^2$ in the plane of p_1 and ϕ_r'' for each fixed ϕ_r'. The minima define saddle point solutions for p_1 and ϕ_r''. Knowing p_1 and ϕ_r'' we find ϕ_i', ϕ_i'', p_2 from Eqs. (1.45,1.46,1.131). Finally, the corresponding harmonic number can be calculated from $\left(\Delta p'\right)^2 = 2(N\omega - I_p)$, yielding $N\omega = A_0^2 \left(p_1 - \sin \phi_r' \cosh \phi_r''\right)^2 / 2 + I_p$. Naturally, the harmonic number defined this way does not have to be integer.

For below threshold harmonics the procedure is essentially the same. For each fixed phi_r' we use equations (1.45,1.46) to express ϕ_i', ϕ_i'' via p_2 and p_1 and then we use Eq.(1.132) to exclude p_1 and substitute $\phi_i'(p_2, \phi_r'')$, $\phi_i''(p_2, \phi_r'')$ and $p_1(p_2, \phi_r'')$ into equations Eqs.1.41,1.42). Using gradient method we can now find the minima of the function $F = F_1^2 + F_2^2$ in the plane of p_2 and ϕ_r'' for each fixed phi_r'. The minima define saddle point solutions for p_2 and ϕ_r''. Knowing p_2 and ϕ_r'' we find ϕ_i', ϕ_i'', p_1 from Eqs. (1.45,1.46,1.132). Finally, the corresponding harmonic number can be calculated from $\left(\Delta p''\right)^2 = 2(I_p - N\omega)$, yielding $N\omega = I_p - A_0^2 \left(p_2 - \sinh \phi_r'' \cos \phi_r'\right)^2 / 2$.

In this method it is convenient to determine the return time ϕ_{tr}' corresponding to the threshold harmonic number $N_t = I_p/\omega$. This can be easily done since at the threshold $p_2 = \sinh(\phi_r'') \cos(\phi_r')$ and $p_1 = \sin(\phi_r') \cosh(\phi_r'')$. Thus we can use these equations together with Eqs.(1.45,1.46) to express ϕ_i', ϕ_i'' via ϕ_r' and ϕ_r'' and then use Eqs. (1.41,1.42) to find a minimum of function $F = F_1^2 + F_2^2$ in the plane of ϕ_r' and ϕ_r'', representing threshold values of ϕ_r' and ϕ_r''. Once the threshold value ϕ_{rt}' of ϕ_r' is known one can separately implement the procedures for below $\phi_r' < \phi_{rt}'$ and above threshold harmonics $\phi_r' > \phi_{tr}'$ described above.

Bibliography

(????) .

Baker et al, S., Y.M.S.P.N.D.D.M.V.P.B.C.M.Y.I. (2006) Probing proton dynamics in molecules on an attosecond time scale. *Science*, **312**, 424.

Brunel, F. (1987) *Phys. Rev. Lett.*, **59**, 52.

Brunel, F. (1990) *J. Opt. Soc. Am. B*, **7**, 521.

Corkum, P.B. (1993) Plasma perspective on strong field multiphoton ionization. *Phys. Rev. Lett*, **71**, 1994.

Corkum et al, P. B., B.N.H.B.F. (1989) *Phys. Rev. Lett.*, **62**, 1259.

Frolov et al, M. V., N.L.M.T.S.S.M.Y.E.M.Y.R.A.F.S. (2009) High-order harmonic generation using intense femtosecond pulses. *Phys Rev Lett*, **102**, 243 901.

Gaarde, Mette B, T.J.L. and Schafer, K.J. (2008) Macroscopic aspects of attosecond pulse generation. *J. Phys. B: At. Mol. Opt. Phys.*, **41**, 132 001.

Grynberg, G., Aspect, A., and Fabre, C. (????) .

Huillier, A. and Balcou, P. (1993) High-order harmonic generation in rare gases with a 1-ps 1053-nm laser. *Phys Rev Lett*, **70**, 774.

Ivanov, M. Yu., B.T. and Burnett, N.H. (1996) *Phys. Rev. A.*, **54**, 742–745.

Krause et al, J. L., K.J.S. and Kulander, K.C. (1992) Xxx. *Phys. Rev. Lett*, **68**, 3535.

Krause et al, J. L., K.J.S.K.C.K. (1992) *Phys. Rev. Lett.*, **68**, 3535.

Krausz, F. and Ivanov, M. (2009) Attosecond physics. *Rev. Mod. Phys.*, **81**, 163.

Kuchiev, M.Y. (1987) Atomic antenna. *Sov. Phys. JETP Letters*, **45**, 319.

Kuchiev, M.Y. and Ostrovsky, V.N. (1999) Quantum theory of high harmonic generation as a three-step process. *Phys Rev A*, **60**, 3111.

Kulander et al, K., K.J.L.K.J.S. (1993) *NATO*, **xx**, xxx.

Lein, M. (2005) Attosecond probing of vibrational dynamics with high-harmonic generation. *Phys Rev Lett*, **94**, 053 004.

Lewenstein et al, M. (1994) Theory of high-harmonic generation by low-frequency laser fields. *Phys. Rev. A.*, **49**, 2117.

Lin et al, C.D., A.T.L.Z.C.T.M.R.L. (2010) High harmonic spectroscopy of multichannel dynamics in strong-field ionization. *J. Phys. B: At. Mol. Opt. Phys.*, **43**, 122 001.

Macklin, J. J., J.D.K. and C. L. Gordon, I. (1993) High-order harmonic generation using intense femtosecond pulses. *Phys Rev Lett*, **70**, 766.

Mairesse et al, Y. (2010) High harmonic spectroscopy of multichannel dynamics in strong-field ionization. *Phys. Rev. Lett.,*, **104**, 213 601.

Morishita, T., L.A.T.C.Z.L.C.D. (2008) Accurate retrieval of structural information from laser-induced photoelectron and high-order harmonic spectra by few cycle pulses. *Phys. Rev. Lett*, **100**, 013 903.

Murray, R., L.W.K. and Yu., I.M. (2010) *Phys. Rev. A.,*, **81**, 023 413.

Murray, R. et al, S.M.P.S.I.M.Y. (2011) *Phys. Rev. Lett.,*, **106**, 173 001.

Perelomov, A.M. and Popov, V.S. (1967) *Sov. Phys. JETP*, **25**, 336.

Perelomov, A. M., P.V.S. and Terent'ev, M.V. (1966) *Sov. Phys. JETP,*, **23**, 924.

Perelomov, A. M., P.V.S. and Terent'ev, M.V. (1967) *Sov. Phys. JETP,*, **24**, 207.

Popov, V. S., K.V.P. and Perelomov, A.M. (1968) *Sov. Phys. JETP,*, **26**, 222.

Schafer et al, K., B.Y.L.F.D.K.C.K. (1993) Above threshold ionization beyond the high

harmonic cutoff. *Phys. Rev. Lett.,*, **70**, 1599.

Smirnova, O., S.M. and Ivanov, M. (2008) *Phys. Rev. A*, **77**, 033 407.

Smirnova et al, O. (2007) *J. Phys. B: At. Mol. Opt. Phys.*, **40**, F197.

Smirnova et al, O., S.M. and Ivanov, M. (2007) Anatomy of strong field ionization ii: to dress or not to dress? *J. Mod. Optics*, **54**, 1019.

Smirnova et al, O., Y.M.S.P.N.D.D.M.V.P.B.C.M.Y.I. (2009) High harmonic interferometry of multi-electron dynamics in molecules. *Nature*, **460**, 972.

Walters, Z. and Smirnova, O. (2010) *J. Phys. B: At. Mol. Opt. Phys.*, **43**, 161 002.

Yudin, G. and Ivanov, M. (2001) Nonadiabatic tunnel ionization: Looking inside a laser cycle. *Phys. Rev. A*, **64**, 013 409.

Zair et al, A. (2008) Quantum path interferences in high-order harmonic generation. *Phys. Rev. Lett.*, **100**, 143 902.